NATIONAL AERONAUTICS AND SPACE ADMINISTRATION

Technical Memorandum 33-620

Molecular Flux Measurements in the Back Flow Region of a Nozzle Plume

J. E. Chirivella

JET PROPULSION LABORATORY
CALIFORNIA INSTITUTE OF TECHNOLOGY
PASADENA, CALIFORNIA

July 15, 1973

Prepared Under Contract No. NAS 7-100
National Aeronautics and Space Administration

PREFACE

The work described in this document was performed by the Propulsion Division of the Jet Propulsion Laboratory.

CONTENTS

CONTENTS (contd)

FIGURES (contd)

FIGURES (contd)

ABSTRACT

A series of tests were conducted at JPL to measure the mass flux in the far field of a nozzle plume in a high vacuum with emphasis on the back flow region. Existing theories to predict the far field of a plume are not adequate for large angular departures from the plume axis. The measurements presented in this report provide fairly accurate data for off-axis angles as large as 140° (i.e., in the back flow region). This region, since it is well behind the exit plane, is of particular interest to those concerned with instrument contamination. Usually sensitive spacecraft surfaces are located in the region affected by the back flow.

The tests, which utilized five different nozzles, were performed at the JPL Molsink facility. Parameters such as expansion ratio, throat diameter, nozzle lip shape, and plenum (chamber) pressure were varied. Carbon dioxide and nitrogen gases were flowed and mass flux measurements were taken using quartz crystal microbalances in as many as nine different locations relative to the test nozzle.

The tests have resulted in a large matrix of data that were correlated and compared to the Hill and Draper flow prediction theory. These tests are a continuation of earlier attempts to provide quantitative data, the results of which were previously published in two JPL reports.

Several conclusions with respect to the effect of nozzle and gas parameters on the amount of back flow mass flux are offered, and it was demonstrated that gaseous mass fluxes, which are not predictable by present theories, are encountered in the region behind the nozzle exit plane. This knowledge is significant if materials incompatible with the gaseous exhaust products are used in this region.

I. INTRODUCTION

Plumes from small attitude propulsion engines as well as from spacecraft main engines have in the past been suspected of impinging on spacecraft surfaces and of causing anomalous behavior of the instrumentation. Existing plume prediction methods fail to give a satisfactory account of the presence of plume gases in the far upstream regions (large plume turning angles) where most instrumentation is located. The problem is increased if the Reynolds number of the internal flow becomes sufficiently small that the boundary layer occupies almost the entire flow field, since it is the gas in the boundary layer which turns beyond the predicted limits.

This phenomena, referred to as boundary layer expansion around the nozzle lip, has been treated in the literature by several investigators (see, for example, Reference (1)). In some instances, as in the cited example, semi-empirical methods are proposed as an expedient to account for the boundary layer effects in the plume far field. However, the criterion of comparison proposed by these methods has been based exclusively on numerical calculations which, although lengthy, fail to include in the modeling the subsonic part of the boundary layer. It is, therefore, highly desirable to obtain accurate experimental data on which to base an empirical theory. The topic of this paper is to present a collection of this type of data obtained recently at the Jet Propulsion Laboratory.

The series of tests reported herein are a continuation of earlier attempts to provide quantitative data on this subject, the results of which have been published in two JPL reports (References (2) and (3)). These tests, which utilized five different nozzles, were performed at the JPL Molecular Sink, high vacuum facility (Molsink). Carbon dioxide and nitrogen were selected as representative gases, and quartz crystal microbalances were used in multiple locations to measure the mass flux in the far field of the plume.

The results presented in this paper are accurate within a few percent and do accurately reflect the physical phenomena which occurs when gases from nozzles with large boundary layers expand into a vacuum. The results were reduced to a form amenable for comparison with existing theories, and it was demonstrated that significant gaseous mass fluxes are encountered in the back flow regions where existing theories are not applicable. These findings are particularly meaningful to those concerned with the effect of rocket exhaust on sensitive surfaces of the spacecraft or on scientific packages that could be directly or indirectly affected by the presence of small traces of exhaust gases.

II. EXPERIMENTAL

A. Facility

One of the major problems associated with the study of vacuum nozzle-plume flow fields has been the sensitivity of the plume far field to the chamber recirculation effects. Since the measurements that this work was concerned with were specifically in the far field, the Molsink facility was selected, as it is an ultra-high vacuum facility capable of cryopumping injected gases at a very high rate. This facility consists of the vacuum chamber and the associated cryogenic systems (see Figure 1). The vacuum chamber encloses two other chambers: the inner liner and the molecular trap. The inner liner is filled with liquid nitrogen that acts as a massive heat sink. The molecular trap (moltrap), the innermost chamber, is a sphere approximately 3 m (10 ft) in diameter, maintained at a temperature between 10 and 15°K with gaseous helium. The walls of the moltrap are wedge-shaped, resembling an anechoic chamber, with a total surface area of approximately 186 m^2 (2000 ft^2). The liquid nitrogen is supplied to the inner liner from a central tank, and vented to the atmosphere. The moltrap is cooled by a manifold of tubes within which gaseous helium at approximately 7°K circulates. The helium is kept at this very low temperature by a refrigerator located adjacent to the chamber. The behavior of a rocket plume inside the Molsink can be described by comparing the flow field both in space and inside the chamber (see Figure 2). The rocket exhaust in space expands freely in an almost radial flow. If a hypothetical perfect sink surface were to enclose such a plume, the flow field enclosed by such a surface would be identical to the one experienced in space. This is

the working principle of the Molsink chamber. However, since the walls of the chamber are not perfect sinks, a small molecular reflection occurs. This reflection results in a recirculation effect that could degrade the space simulation. Since the reflection coefficient depends on the vaporization rate of the gases at the wall temperature and diminishes as the wall temperature is decreased, the vaporization rate of the gases used in these measurements, N_2 and CO_2, is for all practical purposes negligible at 10°K. More information on the facility is available in References (4) to (6).

B. Test Apparatus

In order to assess the effect of nozzle parameters on the plume far field characteristics, five different nozzles were fabricated. Each nozzle was provided with its own cylindrical plenum as shown in Figure 3. The plenum was connected to a length of heavy wall tube 2.13 m (7 ft) long as shown in the figure. For each of these five nozzles a thermocouple and a pressure tap were installed on the plenum, and a coaxial heater was introduced into the connecting tube to provide adequate thermal environment to the tube-plenum-nozzle assembly. The terminals of the plenum pressure tap, heater, and thermocouple were rigidly fixed to the plenum. At the other end of the tube the instrumentation was inserted through leak-proof feed-throughs which were part of the tubing assembly. In this manner, the tube-plenum-nozzle assembly and its instrumentation constituted an independent unit.

The fluid wetted surfaces of each of these units were reproduced as close as possible in order to maintain the same conditions upstream of the nozzle throat. The units were installed into the chamber by introducing the entire set through the Molsink top door. The axis of each of the five nozzles was positioned in a pentagonal pattern as shown in Figure 4. They were held in place by a perforated aluminum plate and its feed-through inserts. The aluminum plate assumed the role of the upper door, and an additional guide for each of the tubes was provided by a perforated plate of micarta that fitted the aperture at the top of the moltrap. With this arrangement each of the five units could be moved up and down and still maintain a very small tolerance for lateral departure. The tubes were fed through tight neoprene fittings which were installed in each hole in the aluminum plate. Lubrication for the tube motion was provided by DC-11, a low outgassing vacuum oil lubricant. The end of each tube outside the Molsink was sealed with a hand valve. The

gases were obtained from bottles located on top of the chamber and injected into the tube-plenum-nozzle unit by means of a combination of regulator and pressure gauges. The thermocouples were connected into the data system and the pressures were recorded from pressure transducers connected to the pressure tap terminals. Table I summarizes the characteristics of these nozzles.

C. Instrumentation

Quartz crystal microbalances (QCM) were used to measure the mass flux in the plume far field, which will be defined herein as all distances greater than 20 exit diameters from the nozzle.

A QCM consists of an electronic oscillator whose resonance frequency is stabilized by the piezoelectric effect of a quartz crystal. The resulting resonance frequency depends on several parameters, but if one fixes the oscillator circuit constants and polarization voltages, the specific modes of crystal vibration will depend only on the orientation of the cut plane with respect to the crystal axes. Depending on the angle of the crystal cut, the precise resonance frequencies will be a function of both the mass deposited on the surface of the crystal and the temperatures. If the crystal experiences a ΔT variation in temperature and a ΔM mass variation, the frequency shift can be expressed as:

$$\Delta f = C_M \Delta M + C_T \Delta T$$

where C_M and C_T depend on the temperature and cut angles of the crystals (see Nomenclature). If a cut angle is chosen such that $C_T = 0$ for some range of temperatures, then $\Delta f = C_M \Delta M$ and the crystal can be used as a delicate microbalance to detect and measure small masses deposited on the surface. Since for a considerable change in temperature and cut angle of the crystal selected, the mass coefficient does not vary more than ±5%, one can use, for all practical purposes, the expression

$$\Delta M = 4.30 \times 10^{-7} \frac{\Delta f}{F_c^2} \qquad (1)$$

where M = mass deposits in g/cm^2, f = frequency shift in Hz, and F_c = resonant frequency in MHz.

An illustration of the crystal, along with the location of one of the electrodes and the thickness vibration mode, can be seen in Figure 5. Additional information related to QCM theory can be found in Reference (4).

The crystal as described in the above paragraph will trap a gas by condensation if its surface is exposed to the flow and its temperature kept well below the condensation temperature of the oncoming gases. Since nitrogen and carbon dioxide were used for this set of experiments, temperatures as low as 15°K were used in order to maintain a very low evaporation rate. Thus, a particular crystal cut with a large C_M coefficient and a low C_T coefficient at temperatures below 15°K had to be determined. It was found that an AT crystal with a cut angle of 40° 28' had very small change in resonance frequency when its temperature was changed by ±10°K while submerged in liquid helium. An oscillator circuit was also designed to operate at low temperatures in high vacuum. The oscillator was kept warmer than the walls by spot heaters installed in its chassis. The crystal was provided with two vacuum deposited gold electrodes which were connected to the oscillator by a coaxial cable long enough to absorb the temperature jump between the oscillator package and crystal. Its length, however, was limited by the noise introduced in the oscillator, since such a lead tends to act like an antenna. Based on this type of mounting, the frequency was stabilized in high vacuum and low temperatures to one part per 5×10^7, which corresponds to a sensitivity of more than a molecular layer.

In order to maintain the crystal temperatures as close as possible to the wall temperature, a U-shaped copper plate was adopted for the crystal chassis. Four crystals were mounted on the plate by two diagonally opposed, low outgassing, silver epoxy spots (see Figure 6a). The front side of the copper plate was provided with four holes of 1.77 cm (0.5 in.) diameter to expose the area of the crystal that was covered by the electrode (see Figure 6b). A complete set of four crystals with the block of remote oscillators can be seen in Figure 6c. The copper plate was provided with spot heaters and a germanium thermistor, allowing for the thermal control necessary for the testing. The thermal control will be described in the Procedures section. The plate was clamped around the gaseous helium tubing that refrigerates the molecular trap, using indium to improve the joint conductance. Two of these sets of crystals were prepared and installed in the locations indicated in Figure 7 and identified as crystal group I and II. Group III referred to in the

same figure corresponds to a different QCM design that will not be described in detail in this paper. It consists of a temperature compensated QCM that can be operated in a range of temperatures of more than 100°K. It is described in complete detail in Reference (8). Figure 7 also shows all the dimensions involved in the test set up and used in the reduction of the data for this paper.

III. PROCEDURES

The output of the crystals was fed into a frequency counter and recorded. The data systems utilized are the same as described in Reference (8) although no filter was necessary for this test series to clean the crystal output signals. The digitized signals were recorded on paper tape, and a different file was opened for each run.

The variables considered in each run consisted of a nozzle type, its vertical position, kind of gas, and plenum pressure level. Prior to the run, the selected nozzle was warmed to room temperature by the coaxial heater and its temperature was stabilized by a slight flow of gas. The plenum pressure was then set to the desired level and the crystal data was recorded for about one to two minutes, at the end of which the gas valve was shut. Recording of the crystal outputs then continued for some time to check for possible desorption. Since the number of tests was so large, the sensitivity of the crystals was affected from time to time by the amount of mass deposited on them. It then became necessary to stop the test momentarily and warm up the crystals by energizing the heaters provided for each crystal package. In this manner a fast thermal desorption allowed for a quick and practical clean-up and recovery of the crystal, which was ready to operate again one hour after its heater was turned back to the off position.

All the systems operated nominally and the total series of tests was accomplished in eight days. At no time was it necessary to pump out the chamber gases, although at the end of the test the background pressure had decayed to 2×10^{-4} N/m^2 (1.5×10^{-6} torr) from an initial value of 2×10^{-10} N/m^2 (1.5×10^{-12} torr).

IV. RESULTS

The results presented in this paper are summarized in Table II. Each of the five nozzles was tested with carbon dioxide and nitrogen, and each gas was run at several plenum pressures. Furthermore, each case was run for two or three different positions of the nozzle, varying the relative position of the plenum with respect to the QCMs. All nozzles were run at approximately 294°K (70°F) plenum temperature.

The cases described in Table II were analyzed by grouping the cases that differ only in the distance of the nozzle to the Molsink top. The raw data is presented as an array in which the frequency of each QCM is tabulated versus time. From this table and by using Equation 1, the following equation is obtained:

$$\frac{\dot{M}}{A_c} = \frac{\text{mas flux rate arriving at the crystal}}{\text{area of the crystal}} \approx \frac{d\dot{M}}{dA_c}$$

Furthermore, dA_c can be expressed as

$$dA_c = r^2 \cos\phi \, d\Omega$$

where r is the distance from the nozzle exit section to the center of the crystal, ϕ is the angle between the normal to the crystal and $\vec{r}$, and $d\Omega$ is the solid angle substended by dA_c from the center of the nozzle exit section. From this expression one obtains

$$\left(\frac{d\dot{m}}{d\Omega}\right)_\theta = \text{mass flux per unit solid angle} \approx \frac{\dot{M}}{A_c} \frac{r^2}{\cos\phi}$$

where θ is the angular distance from the crystal to the plume axis. If one normalizes this by its value at the axis, one obtains

$$\left(\frac{d\dot{m}}{d\Omega}\right)_\theta \Big/ \left(\frac{d\dot{m}}{d\Omega}\right)_{\theta = 0} = f(\theta)$$

The function $f(\theta)$ has received considerable attention in the literature, and the data in this paper has been reduced to provide information about this function. The value of $(dm/d\Omega)_{\theta = 0}$ obtained by the Hill and Drapper scheme (Reference (9)) has been adopted, and the resulting data compared with the $f(\theta)$ proposed by those investigators, i.e.,

$$f(\theta) = \exp \left\{-\left[\lambda^2(1 - \cos \theta)^2\right]\right\}$$

where

$$\lambda = \left[\pi^{1/2}(1 - C_F/C_{FMAX})\right]^{-1}$$

is the plume slenderness coefficient, and

$$\left(\frac{d\dot{m}}{d\Omega}\right)_{\theta = 0} = \frac{\dot{m}_w \lambda}{\pi^{3/2}}$$

is the mass normalization factor at the axis center line and $\dot{m}_w$ = nozzle total mass flow rate. The data is being presented in Figures 8 to 17 in semi-logarithmic scale, i.e.,

$$f(\theta) = 10^{-K_M(\theta)}$$

where K_M is the mass coefficient. The normalization factor $(d\dot{m}/d\Omega)_{\theta = 0}$ is also given for convenience. Tables II to VII contain the numerical values of K_M for several θ's. Because of the logarithmic characteristics of the ordinate, the cases corresponding to different pressures for the same nozzle-gas combination have been grouped together.

V. DISCUSSION

The results described in the above paragraphs constitute a representative sampling of the total amounts of data obtained. In the majority of cases, the data is accurate within ±5% as measured by the QCMs. There are, however, some cases in which the QCMs readings were relatively poor, and they

have been marked in Table II by an asterisk. Nevertheless, these cases were the exception and were mostly due to QCM saturation because of cumulative mass deposits and are easy to detect and identify.

A question arises about the correlation between the mass flux as registered by the crystal and the actual mass flux impinging on the crystal surface. In order to check such a correlation, QCMs frequencies were compared before and after closing the gas valve. While the QCM presented a constantly decreasing frequency before closing the hand valve, the frequency was stabilized immediately to its last value once the hand valve was closed. This behavior indicates that all the mass arriving to the crystal was instantly captured by its surface, as was expected because of the low crystal temperature as compared with the nitrogen condensation temperature. Migration effects, on the other hand, were responsible for dumping relatively large amounts of mass from the copper plate onto the crystals, but these rates were extremely slow as compared with the plume gas deposition, and they only caused saturation problems and signal modulations with periods on the order of hours.

One peculiarity easily observed in Figures 8 and 9 is the fact that different groupings of data are obtained for the same plume under different relative positions within the chamber and respect to QCMs. It is interesting to note that the intermediate grouping corresponds in both runs to the lowest position of the nozzle, i.e., 60.96 cm (2.0 ft.) from the top, the upper grouping corresponds to the intermediate position of the nozzle (45.72 cm, 1.5 ft.) and the lower one to the highest position (30.28 cm, 1.0 ft.). The reason for this is not well understood as yet, but could be caused by different QCM sensitivities (quite improbable), by different residual recirculation effects (not consistent with the relative position of the groupings of data), and/or gas surface effects at the nozzle lip (these effects are randomly distributed and are inconsistent with the organized order encountered in Figures 8 and 9). This question will be left open at this time, although the data scatter does not appear too adverse. Because of the small expansion ratio of Nozzle 1, the location of the data approaches that region of the plume in which the boundary layer correction departure from the inviscid theory begins, which shows that the QCMs readings are consistent with the theory in the region of the theory's validity. A comparison of Figures 10 and 14, and 11 and 15, shows the effects of a flat nozzle edge versus a sharp edge. It can be seen

that the nozzle with a sharp edge, as expected, spills more mass in the back region than the flat edged one. The same scattering mentioned before can be observed here. Note also that, in most cases, an increase in pressure reduces the back flow mass flux, although this effect seems to be less accentuated than the data spread due to the geometrical position of the plume in the chamber.

In Figures 12 and 13 one can see that the high expansion ratio of the nozzle produces a very slender theoretical plume. However, the back flow mass flux is little affected by the high expansion rates and thus remains of the same order of magnitude as in the cases previously mentioned. Figures 16 and 17 show the effect of the conical angle. Comparison with Figures 10 and 11 does not indicate any outstanding difference between a 15° or a 25° cone angle, except in those regions closer to the axis where the data tends to increase or decrease with the cone angle. This variation is probably due to two dimensional effects at the exit plane.

VI. SUMMARY

Forty-four cases of back flow measurements have been reported. Although some data spread is observed, enough information is presented to show the order of magnitude involved in the correction of existing theories. This set of data is the most comprehensive ever obtained and provides an answer to the many expressed concerns with estimates of exhaust gases in those regions of the plume that depart more than 90° from the center line. This could be of significance if materials incompatible with the gaseous exhaust products are used in this vicinity, or if a science experiment conducted in these regions could be affected by the presence of these gases.

VII. CONCLUSIONS

From the previous discussion, one concludes:

(1) The cryogenic QCMs appear to be the ideal type of instrument to perform plume far field mass flux measurements.

(2) The back flow measurements seem to converge to the predicted theoretical values for smaller departures from the plume axis.

(3) The specific heat ratio and/or molecular weight of the gas does not seem to affect the data drastically.

(4) A plenum pressure increase reduces the mass flux into the back flow region.

(5) The flat edge acts as a molecular beam deflector; that is, it screens the back flow region from molecular bombardment.

(6) The cone angle of the nozzle affects only that data which is relatively close to the axis.

(7) A large expansion ratio does not affect the back flow mass flux.

As a result of these conclusions, it is inferred that the mechanisms of gas-surface interaction that take place at the nozzle edge may be dictating the amount of mass flux expected for large departure angles (over 100°), while the boundary layer expansion may regulate the far field structure from 40° to 100°

NOMENCLATURE

A_c = area of the crystal (cm^2)

C_F = thrust coefficient

C_M = crystal mass coefficient $\left(\frac{\partial f}{\partial M}\right)_T$, (Hz cm^2/g)

C_T = crystal temperature coefficient $\left(\frac{\partial f}{\partial T}\right)_M$, (Hz/°K)

F_c = average crystal frequency, (MHz)

f = crystal frequency, (Hz)

K_M = back flow mass flux coefficient

M = mass deposit on crystal (g/cm^2)

$\dot{M}$ = mass flux rate arriving at the crystal ($g/cm^2/sec$)

$\dot{m}(\theta)$ = mass flux rate at θ location, ($g/cm^2/sec$)

$\vec{r}$ = radius vector from the nozzle exit plane center to the crystal center

r = $\left|\vec{r}\right|$, (cm)

s = nozzle edge width (cm)

λ = plume slenderness parameter

ϕ = angle between the normal to the crystal and the radius vector r

Ω = solid angle

θ = angular distance from plume axis

REFERENCES

1. Simmons, G. A., "Effects of Nozzle Boundary Layers on Rocket Exhaust Plumes", A.I.A.A. Journal, Vol. 10, No. 11, November, 1972, p. 1535.

2. Simon, W., "Plume Backscatter Measurements Using Quartz Crystal Microbalances in JPL Molsink (Molecular Sink)", JPL TM 33-540, dated May 15, 1972.

3. Chirivella, J. E., Moynihan, P. I., Simon, W., "Small Rocket Exhaust Plume Data", JPL Quarterly Technical Review, Volume 2, Number 2, dated July, 1972.

4. Stephens, J. B., "Spacecraft Mechanism Testing in the Molsink Facility", paper presented at the 4th Aerospace Symposium, University of Santa Clara, May 22-23, 1969.

5. Stephens, J. B., "Molecular Sink", Research/Development, July, 1967.

6. Stephens, J. B., "Space Molecular Sink Simulator Facility Design", J. Spacecraft Rockets, June, 1966.

7. Sauerbrey, G., "Use of Oscillator Quartz Crystals for Weighing Thin Layers and Microweighing", Ann. Physik, Vol. 155, pp. 206-222, 1959.

8. Chirivella, J. E., and Moynihan, P. I., "Hydrazine Rocket Engine Plume Deposits Measured with Quartz Crystal Microbalances", 7th JANNAF Plume Technology Meeting.

9. Hill, J. A. F., and Draper, J. S., "Analytical Approximation for the Flow from a Nozzle into a Vacuum", J. Spacecraft Rockets, Vol. 3, No. 10, pp. 1552-1559, October, 1966.

Table I. Geometric characteristics of the five tested nozzles

Nozzle	Expansion ratio ϵ	Throat diameter cm (in.)	Cone angle degrees	Throat area cm^2 ($in.^2$)	Lip widths cm (in.)
1	15.0	0.508 (0.2)	25.0	0.203 (0.0314)	0.254 (0.1)
2	60.0	0.254 (0.1)	25.0	0.051 (0.00785)	0.254 (0.1)
3	240.0	0.177 (0.05)	25.0	0.0126 (0.00196)	0.254 (0.1)
4	60.0	0.254 (0.1)	25.0	0.051 (0.00785)	0.0 (0.0)
5	60.0	0.254 (0.1)	15.0	0.051 (0.00785)	0.254 (0.1)

Table II. Summary of cases presented and analyzed

Case No.	Nozzle	Gas	Pressure N/m^2 (psia)	Distance from Molsink top-cm (in.)
1	1	N_2	2.19×10^4 (3.2)	30.48 (12)
2	1	N_2	2.19×10^4 (3.2)	45.72 (18)
3	1	N_2	2.19×10^4 (3.2)	60.96 (24)
4	1	CO_2	2.19×10^4 (3.2)	30.48 (12)
5*	1	CO_2	2.19×10^4 (3.2)	45.72 (18)
6	1	CO_2	2.19×10^4 (3.2)	60.96 (24)
7*	2	N_2	2.19×10^4 (3.2)	66.04 (26)
8*	2	N_2	8.5×10^4 (12.4)	45.72 (18)
9	2	N_2	1.2×10^5 (17.5)	45.72 (18)
10*	2	CO_2	2.19×10^4 (3.2)	45.72 (18)
11	2	CO_2	2.19×10^4 (3.2)	66.04 (26)
12	2	CO_2	8.5×10^4 (12.4)	45.72 (18)
13*	2	CO_2	1.2×10^5 (17.5)	45.72 (18)
14	3	N_2	2.19×10^4 (3.2)	60.96 (24)
15	3	N_2	8.5×10^4 (12.4)	60.96 (24)
16	3	N_2	1.2×10^5 (17.5)	60.96 (24)
17	3	CO_2	2.19×10^4 (3.2)	60.96 (24)
18	3	CO_2	8.5×10^4 (12.4)	60.96 (24)
19	3	CO_2	1.7×10^5 (25.0)	60.96 (24)
20	4	N_2	2.19×10^4 (3.2)	45.72 (18)
21	4	N_2	2.19×10^4 (3.2)	66.04 (26)
22	4	N_2	8.5×10^4 (12.4)	45.72 (18)
23	4	N_2	8.5×10^4 (12.4)	66.04 (26)

*Cases suspected of containing some poor QCM readings

Table II (contd)

Case No.	Nozzle	Gas	Pressure N/m^2 (psia)	Distance from Molsink top-cm (in.)
24	4	N_2	8.5×10^4 (12.4)	91.44 (36)
25	4	N_2	1.2×10^5 (17.5)	45.72 (18)
26	4	N_2	1.2×10^5 (17.5)	66.04 (26)
27	4	N_2	1.2×10^5 (17.5)	91.44 (36)
28*	4	CO_2	2.19×10^4 (3.2)	66.04 (26)
29*	4	CO_2	2.19×10^4 (3.2)	91.44 (36)
30	4	CO_2	8.5×10^4 (12.4)	66.04 (26)
31	4	CO_2	1.2×10^5 (17.5)	66.04 (26)
32	4	CO_2	1.2×10^5 (17.5)	91.44 (36)
33	5	N_2	2.19×10^4 (3.2)	50.8 (20)
34*	5	N_2	2.19×10^4 (3.2)	76.2 (30)
35	5	N_2	8.5×10^4 (12.4)	50.8 (20)
36	5	N_2	8.5×10^4 (12.4)	76.2 (30)
37	5	N_2	1.2×10^5 (17.5)	50.8 (20)
38*	5	N_2	1.2×10^5 (17.5)	76.2 (30)
39	5	CO_2	2.19×10^4 (3.2)	50.8 (20)
40	5	CO_2	2.19×10^4 (3.2)	76.2 (30)
41	5	CO_2	8.5×10^4 (12.4)	50.8 (20)
42	5	CO_2	8.5×10^4 (12.4)	76.2 (30)
43	5	CO_2	1.2×10^5 (17.5)	50.8 (20)
44*	5	CO_2	1.2×10^5 (17.5)	76.2 (30)

*Cases suspected of containing some poor QCM readings

Table III. Numerical values of back flow mass coefficient K_M versus θ for Nozzle 1

$\left(\frac{d\dot{m}}{d\Omega}\right)_\theta \Big/ \left(\frac{d\dot{m}}{d\Omega}\right)_{\theta = 0} = f(\theta) = 10^{-K_M}$	Nitrogen
Plenum pressure 2.19×10^4 N/m^2 (3.2 psia)	$\left(\frac{d\dot{m}}{d\Omega}\right)_{\theta = 0} = 1.48$ g/sec
θ	K_M
50.66	1.90
64.33	2.46
71.43	2.60
73.21	2.68
75.09	2.74
77.06	2.82
85.42	2.32
87.34	3.21
87.62	2.45
89.65	3.28
89.90	2.53
92.16	3.37
92.26	2.65
94.89	3.46
102.32	3.49
104.72	3.55
106.57	3.08
107.16	3.61
109.42	3.14
112.40	3.22
115.52	3.28
122.69	3.99
125.41	4.03
131.00	4.12

Table III (contd)

$\left(\frac{d\dot{m}}{d\Omega}\right)_\theta \Big/ \left(\frac{d\dot{m}}{d\Omega}\right)_{\theta = 0} = f(\theta) = 10^{-K_M}$	Carbon dioxide
Plenum pressure 2.19×10^4 N/m^2 (3.2 psia)	$\left(\frac{d\dot{m}}{d\Omega}\right)_{\theta = 0}$ = 3.05 g/sec
θ	K_M
56.97	2.20
64.33	2.72
71.43	2.83
73.21	2.92
75.09	3.00
77.06	3.09
87.34	3.51
89.65	3.57
92.16	3.67
94.89	3.76
102.32	3.73
104.72	3.80
106.57	3.31
107.16	3.85
109.42	3.37
112.40	3.46
115.52	3.54
122.42	4.27
125.42	4.31

Table IV. Numerical values of back flow mass coefficient K_M versus θ for Nozzle 2

$\left(\frac{d\dot{m}}{d\Omega}\right)_\theta \Big/ \left(\frac{d\dot{m}}{d\Omega}\right)_{\theta = 0} = f(\theta) = 10^{-K_M}$	Nitrogen
Plenum pressure 2.19×10^4 N/m^2 (3.2 psia)	$\left(\frac{d\dot{m}}{d\Omega}\right)_{\theta = 0} = 0.585$ g/sec
θ	K_M
67.68	2.93
103.95	4.23
106.19	4.31
108.46	4.28
110.73	4.35
125.31	4.27
127.80	4.27
132.84	4.34
$\left(\frac{d\dot{m}}{d\Omega}\right)_\theta \Big/ \left(\frac{d\dot{m}}{d\Omega}\right)_{\theta = 0} = f(\theta) = 10^{-K_M}$	Nitrogen
Plenum pressure 8.5×10^4 N/m^2 (12.4 psia)	$\left(\frac{d\dot{m}}{d\Omega}\right)_{\theta = 0} = 2.27$ g/sec
θ	K_M
57.81	2.71
85.63	3.29
92.15	4.00
108.22	4.54
113.88	5.46

Table IV (contd)

$\left(\frac{d\dot{m}}{d\Omega}\right)_\theta \Big/ \left(\frac{d\dot{m}}{d\Omega}\right)_{\theta = 0} = f(\theta) = 10^{-K_M}$	Nitrogen
Plenum pressure 1.2×10^5 N/m^2 (17.5 psia)	$\left(\frac{d\dot{m}}{d\Omega}\right)_{\theta = 0} = 3.20$ g/sec
θ	K_M
57.81	2.59
85.63	3.37
92.15	3.89
108.22	4.49
113.88	5.55
$\left(\frac{d\dot{m}}{d\Omega}\right)_\theta \Big/ \left(\frac{d\dot{m}}{d\Omega}\right)_{\theta = 0} = f(\theta) = 10^{-K_M}$	Carbon dioxide
Plenum pressure 2.19×10^4 N/m^2 (3.2 psia)	$\left(\frac{d\dot{m}}{d\Omega}\right)_{\theta = 0} = 1.38$ g/sec
θ	K_M
57.81	2.95
67.68	3.40
85.63	4.45
92.15	4.24
103.95	4.64
105.57	5.15
106.19	4.68
108.22	4.60
108.46	4.72
110.73	4.77
113.88	5.07
125.31	4.89
127.80	4.90
132.84	4.91

Table IV (contd)

$\left(\frac{d\dot{m}}{d\Omega}\right)_\theta \Big/ \left(\frac{d\dot{m}}{d\Omega}\right)_{\theta = 0} = f(\theta) = 10^{-K_M}$	Carbon dioxide
Plenum pressure 8.5×10^4 N/m^2 (12.4 psia)	$\left(\frac{d\dot{m}}{d\Omega}\right)_{\theta = 0} = 5.34$ g/sec
θ	K_M
57.81	2.80
92.15	4.19
108.22	4.75
110.99	5.04
$\left(\frac{d\dot{m}}{d\Omega}\right)_\theta \Big/ \left(\frac{d\dot{m}}{d\Omega}\right)_{\theta = 0} = f(\theta) = 10^{-K_M}$	Carbon dioxide
Plenum pressure 1.2×10^5 N/m^2 (17.5 psia)	$\left(\frac{d\dot{m}}{d\Omega}\right)_{\theta = 0} = 7.53$ g/sec
θ	K_M
57.81	2.46
110.99	5.80
113.88	6.22

Table V. Numerical values of back flow mass coefficient K_M versus θ for Nozzle 3

$\left(\frac{d\dot{m}}{d\Omega}\right)_\theta \Big/ \left(\frac{d\dot{m}}{d\Omega}\right)_{\theta=0} = f(\theta) = 10^{-K_M}$	Nitrogen
Plenum pressure 2.19×10^4 N/m^2 (3.2 psia)	$\left(\frac{d\dot{m}}{d\Omega}\right)_{\theta=0} = 0.227$ g/sec
θ	K_M
66.08	2.74
118.75	3.65
121.14	4.05
$\left(\frac{d\dot{m}}{d\Omega}\right)_\theta \Big/ \left(\frac{d\dot{m}}{d\Omega}\right)_{\theta=0} = f(\theta) = 10^{-K_M}$	Nitrogen
Plenum pressure 8.5×10^4 N/m^2 (12.4 psia)	$\left(\frac{d\dot{m}}{d\Omega}\right)_{\theta=0} = 0.879$ g/sec
θ	K_M
66.08	3.02
118.75	4.10
121.14	4.49
126.06	4.62
$\left(\frac{d\dot{m}}{d\Omega}\right)_\theta \Big/ \left(\frac{d\dot{m}}{d\Omega}\right)_{\theta=0} = f(\theta) = 10^{-K_M}$	Nitrogen
Plenum pressure 1.2×10^5 N/m^2 (17.5 psia)	$\left(\frac{d\dot{m}}{d\Omega}\right)_{\theta=0} = 1.24$ g/sec
θ	K_M
66.08	3.14
118.75	4.20
121.14	4.55
126.06	4.76

Table V (contd)

$\left(\frac{d\dot{m}}{d\Omega}\right)_\theta \Big/ \left(\frac{d\dot{m}}{d\Omega}\right)_{\theta = 0} = f(\theta) = 10^{-K_M}$	Carbon dioxide
Plenum pressure 2.19×10^4 N/m^2 (3.2 psia)	$\left(\frac{d\dot{m}}{d\Omega}\right)_{\theta = 0} = 0.610$ g/sec
θ	K_M
66.08	3.53
105.25	4.09
118.75	4.18
121.14	4.33
$\left(\frac{d\dot{m}}{d\Omega}\right)_\theta \Big/ \left(\frac{d\dot{m}}{d\Omega}\right)_{\theta = 0} = f(\theta) = 10^{-K_M}$	Carbon dioxide
Plenum pressure 1.7×10^5 N/m^2 (25 psia)	$\left(\frac{d\dot{m}}{d\Omega}\right)_{\theta = 0} = 3.34$ g/sec
θ	K_M
66.08	3.02
98.86	4.22
105.25	4.45
118.75	4.67
121.14	4.83
126.06	5.06

Table VI. Numerical values of back flow mass coefficient K_M versus θ for Nozzle 4

$\left(\frac{d\dot{m}}{d\Omega}\right)_\theta \Big/ \left(\frac{d\dot{m}}{d\Omega}\right)_{\theta=0} = f(\theta) = 10^{-K_M}$	Nitrogen
Plenum pressure 2.19×10^4 N/m^2 (3.2 psia)	$\left(\frac{d\dot{m}}{d\Omega}\right)_{\theta=0} = 0.585$ g/sec
θ	K_M
68.63	2.84
85.93	3.53
87.89	3.60
89.91	3.67
92.00	3.76
105.14	3.67
107.25	3.70
109.18	4.34
109.38	3.74
111.80	4.31
122.89	3.83
125.21	3.85
129.95	3.88
$\left(\frac{d\dot{m}}{d\Omega}\right)_\theta \Big/ \left(\frac{d\dot{m}}{d\Omega}\right)_{\theta=0} = f(\theta) = 10^{-K_M}$	Nitrogen
Plenum pressure 8.5×10^4 N/m^2 (12.4 psia)	$\left(\frac{d\dot{m}}{d\Omega}\right)_{\theta=0} = 2.267$ g/sec
θ	K_M
59.03	2.89
82.57	3.42
85.93	3.60
87.89	3.67
89.91	3.74
91.99	3.80
104.27	4.29
105.13	3.91
106.67	4.37
107.25	3.94
109.38	3.97
121.39	4.65
122.88	4.13
123.21	4.71
125.01	4.74
125.21	4.15

Table VI (contd)

$\left(\frac{d\dot{m}}{d\Omega}\right)_\theta \Big/ \left(\frac{d\dot{m}}{d\Omega}\right)_{\theta=0} = f(\theta) = 10^{-K_M}$	Nitrogen
Plenum pressure 8.5×10^4 N/m^2 (12.4 psia)	$\left(\frac{d\dot{m}}{d\Omega}\right)_{\theta=0}$ = 2.267 g/sec
θ	K_M
126.79	4.82
129.95	4.19
138.66	4.89
140.51	4.95
144.16	5.00
$\left(\frac{d\dot{m}}{d\Omega}\right)_\theta \Big/ \left(\frac{d\dot{m}}{d\Omega}\right)_{\theta=0} = f(\theta) = 10^{-K_M}$	Nitrogen
Plenum pressure 1.2×10^5 N/m^2 (17.5 psia)	$\left(\frac{d\dot{m}}{d\Omega}\right)_{\theta=0}$ = 3.20 g/sec
θ	K_M
68.63	2.92
82.57	3.39
85.93	3.50
87.89	3.58
89.91	3.65
92.00	3.71
104.27	4.17
105.13	3.86
106.67	4.24
107.25	3.90
109.38	3.94
121.39	4.60
122.89	4.12
123.21	4.66
125.01	4.73
125.21	4.14
126.69	4.77
129.95	4.18
138.67	4.95
140.51	5.04
144.16	5.09

Table VI (contd)

$\left(\frac{d\dot{m}}{d\Omega}\right)_\theta \Big/ \left(\frac{d\dot{m}}{d\Omega}\right)_{\theta = 0} = f(\theta) = 10^{-K_M}$	Carbon dioxide
Plenum pressure 2.19×10^4 N/m^2 (3.2 psia)	$\left(\frac{d\dot{m}}{d\Omega}\right)_{\theta = 0}$ = 1.38 g/sec
θ	K_M
68.63	3.18
82.57	3.72
105.14	4.04
107.25	4.06
109.38	4.09
121.39	4.98
123.21	5.10
125.01	5.26
125.21	4.25
126.79	5.25
127.57	5.31
138.67	5.35
140.51	5.59
144.17	5.57
$\left(\frac{d\dot{m}}{d\Omega}\right)_\theta \Big/ \left(\frac{d\dot{m}}{d\Omega}\right)_{\theta = 0} = f(\theta) = 10^{-K_M}$	Carbon dioxide
Plenum pressure 8.5×10^4 N/m^2 (12.4 psia)	$\left(\frac{d\dot{m}}{d\Omega}\right)_{\theta = 0}$ = 5.34 g/sec
θ	K_M
68.63	3.22
105.14	4.12
107.25	4.15
109.38	4.19
122.89	4.39
125.21	4.41

Table VI (contd)

$\left(\frac{d\dot{m}}{d\Omega}\right)_\theta \Big/ \left(\frac{d\dot{m}}{d\Omega}\right)_{\theta = 0} = f(\theta) = 10^{-K_M}$	Carbon dioxide
Plenum pressure 1.2×10^5 N/m^2 (17.4 psia)	$\left(\frac{d\dot{m}}{d\Omega}\right)_{\theta = 0} = 7.53$ g/sec
θ	K_M
68.63	3.06
82.57	3.54
105.14	3.93
107.25	3.96
109.38	4.00
121.39	4.65
122.89	4.19
123.21	4.70
125.01	4.78
125.21	4.20
126.80	4.82
138.67	5.21
140.51	5.24
144.17	5.41

Table VII. Numerical values of back flow mass coefficient K_M versus θ for Nozzle 5

$\left(\frac{d\dot{m}}{d\Omega}\right)_\theta \Big/ \left(\frac{d\dot{m}}{d\Omega}\right)_{\theta=0} = f(\theta) = 10^{-K_M}$	Nitrogen
Plenum pressure 2.19×10^4 N/m^2 (3.2 psia)	$\left(\frac{d\dot{m}}{d\Omega}\right)_{\theta=0} = 0.585$ g/sec
θ	K_M
60.11	2.68
92.46	3.92
94.70	3.98
97.00	4.09
111.11	4.51
112.33	3.64
113.78	4.58
114.48	3.71
116.63	3.72
118.77	3.76
119.42	4.72
132.71	3.84
134.97	3.85
139.47	3.97
$\left(\frac{d\dot{m}}{d\Omega}\right)_\theta \Big/ \left(\frac{d\dot{m}}{d\Omega}\right)_{\theta=0} = f(\theta) = 10^{-K_M}$	Nitrogen
Plenum pressure 8.5×10^4 N/m^2 (12.4 psia)	$\left(\frac{d\dot{m}}{d\Omega}\right)_{\theta=0} = 2.27$ g/sec
θ	K_M
60.11	2.95
73.24	3.22
92.46	3.96
94.70	4.03
97.00	4.13
111.11	4.76
113.76	4.89
114.48	4.12
116.63	4.16
118.77	4.18
119.42	5.13
132.71	4.27
134.97	4.29
139.47	4.59

Table VII (contd)

$\left(\frac{d\dot{m}}{d\Omega}\right)_\theta \Big/ \left(\frac{d\dot{m}}{d\Omega}\right)_{\theta = 0} = f(\theta) = 10^{-K_M}$	Nitrogen
Plenum pressure 1.2×10^5 N/m^2 (17.5 psia)	$\left(\frac{d\dot{m}}{d\Omega}\right)_{\theta = 0} = 3.20$ g/sec
θ	K_M
60.11	2.88
73.24	3.27
92.46	3.89
94.70	3.97
97.00	4.05
111.11	4.69
113.78	4.81
114.48	4.20
116.63	4.23
118.77	4.25
119.42	5.08
132.71	4.37
134.97	4.38
139.47	4.88
$\left(\frac{d\dot{m}}{d\Omega}\right)_\theta \Big/ \left(\frac{d\dot{m}}{d\Omega}\right)_{\theta = 0} = f(\theta) = 10^{-K_M}$	Carbon dioxide
Plenum pressure 2.19×10^4 N/m^2 (3.2 psia)	$\left(\frac{d\dot{m}}{d\Omega}\right)_{\theta = 0} = 1.38$ g/sec
θ	K_M
60.11	3.14
73.24	3.28
92.46	4.19
94.70	4.29
97.00	4.38
111.11	4.93
112.33	4.16
113.78	5.05
114.48	4.18
116.63	4.21
118.77	4.23
119.42	5.22
132.71	4.41
134.97	4.34
137.22	4.43
139.47	4.52

Table VII (contd)

$\left(\frac{d\dot{m}}{d\Omega}\right)_\theta \Big/ \left(\frac{d\dot{m}}{d\Omega}\right)_{\theta = 0} = f(\theta) = 10^{-K_M}$	Carbon dioxide
Plenum pressure 8.5×10^4 N/m^2 (12.4 psia)	$\left(\frac{d\dot{m}}{d\Omega}\right)_{\theta = 0} = 5.34$ g/sec
θ	K_M
60.11	3.17
73.24	3.40
92.46	4.22
94.70	4.30
97.00	4.38
111.11	4.99
112.33	4.40
113.78	5.11
114.48	4.44
116.63	4.49
118.77	4.51
119.42	5.33
134.97	4.66
139.47	4.69
$\left(\frac{d\dot{m}}{d\Omega}\right)_\theta \Big/ \left(\frac{d\dot{m}}{d\Omega}\right)_{\theta = 0} = f(\theta) = 10^{-K_M}$	Carbon dioxide
Plenum pressure 1.2×10^5 N/m^2 (17.5 psia)	$\left(\frac{d\dot{m}}{d\Omega}\right)_{\theta = 0} = 7.53$ g/sec
θ	K_M
60.11	2.89
73.24	3.40
92.46	4.00
94.70	4.09
97.00	4.16
111.11	4.72
112.33	4.35
113.78	4.83
114.48	4.40
116.63	4.44
118.77	4.47
119.42	5.04
134.97	4.60
139.47	4.69

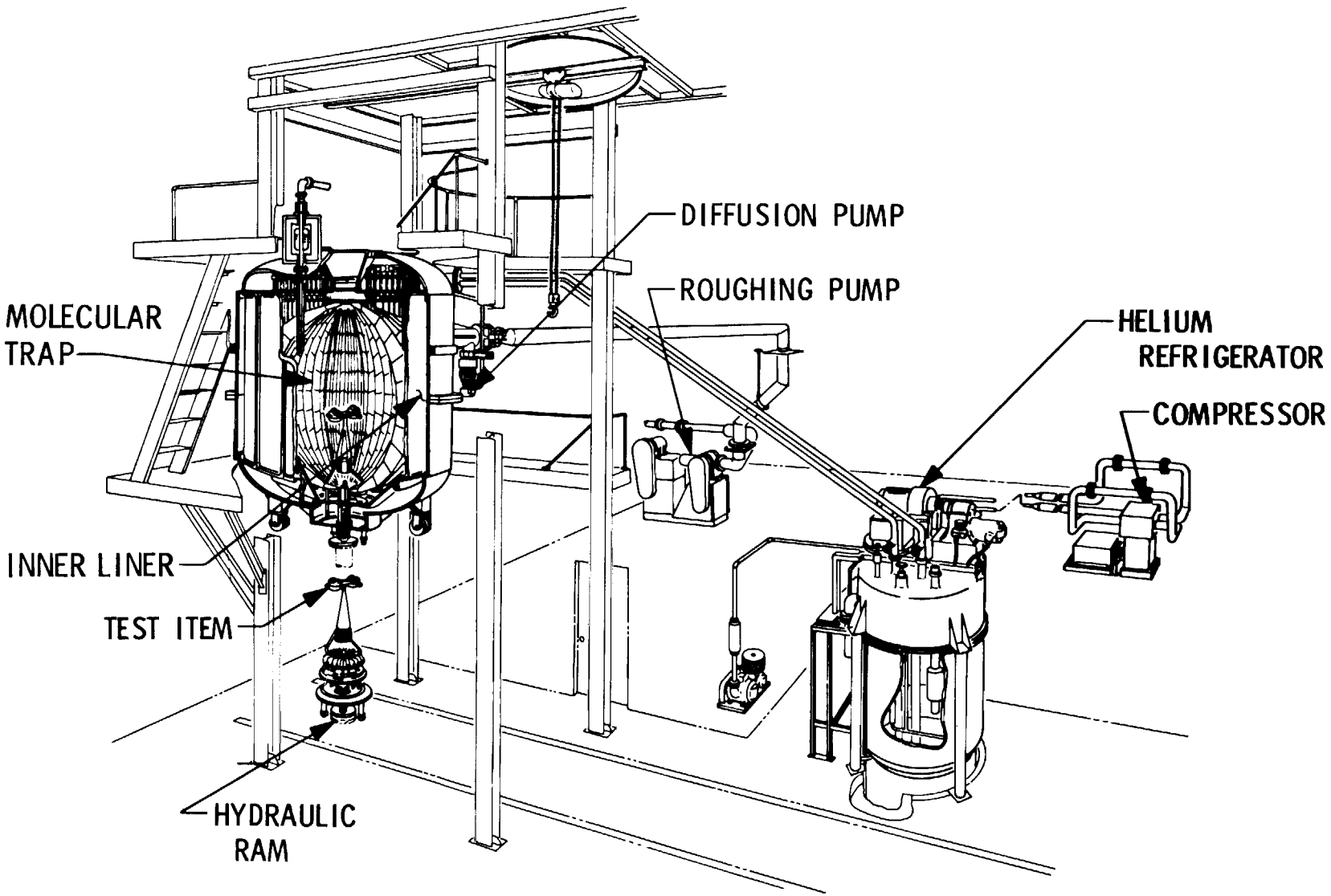

Fig. 1. Molsink vacuum chamber and auxiliary equipment

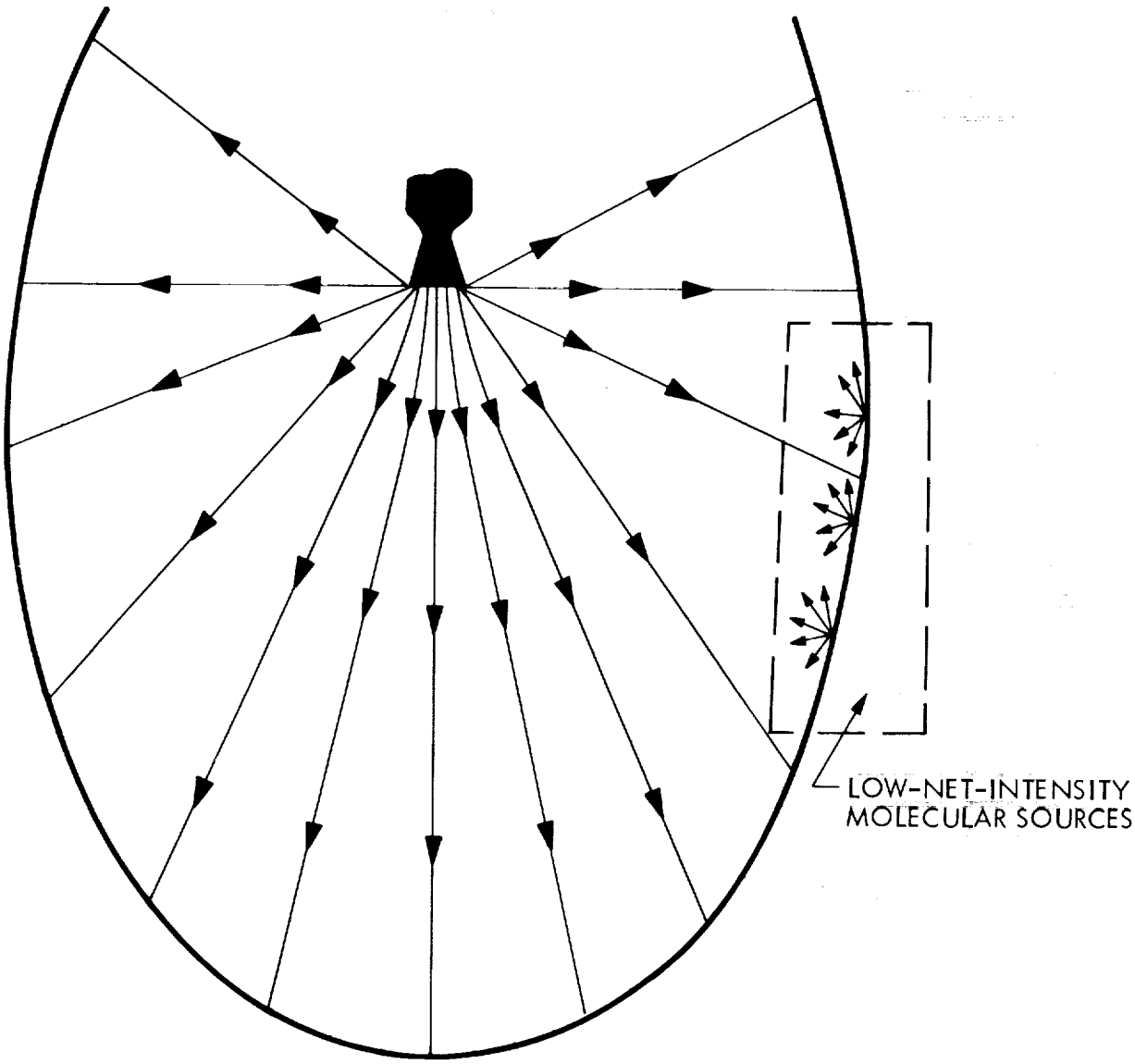

Fig. 2. Rocket Plume in Molsink chamber

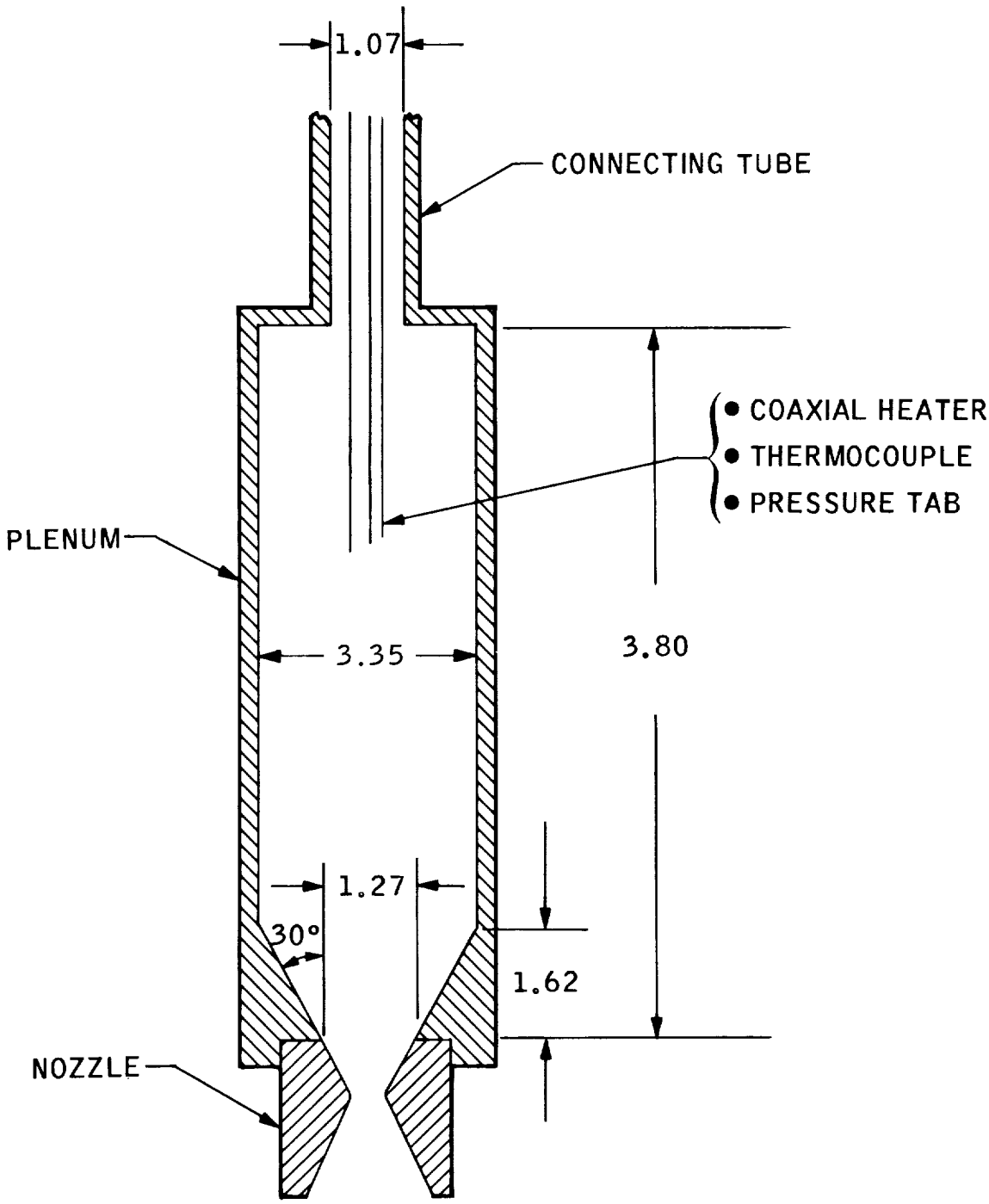

Fig. 3. Nozzle-plenum assembly installed in the Molsink (all dimensions are in cm)

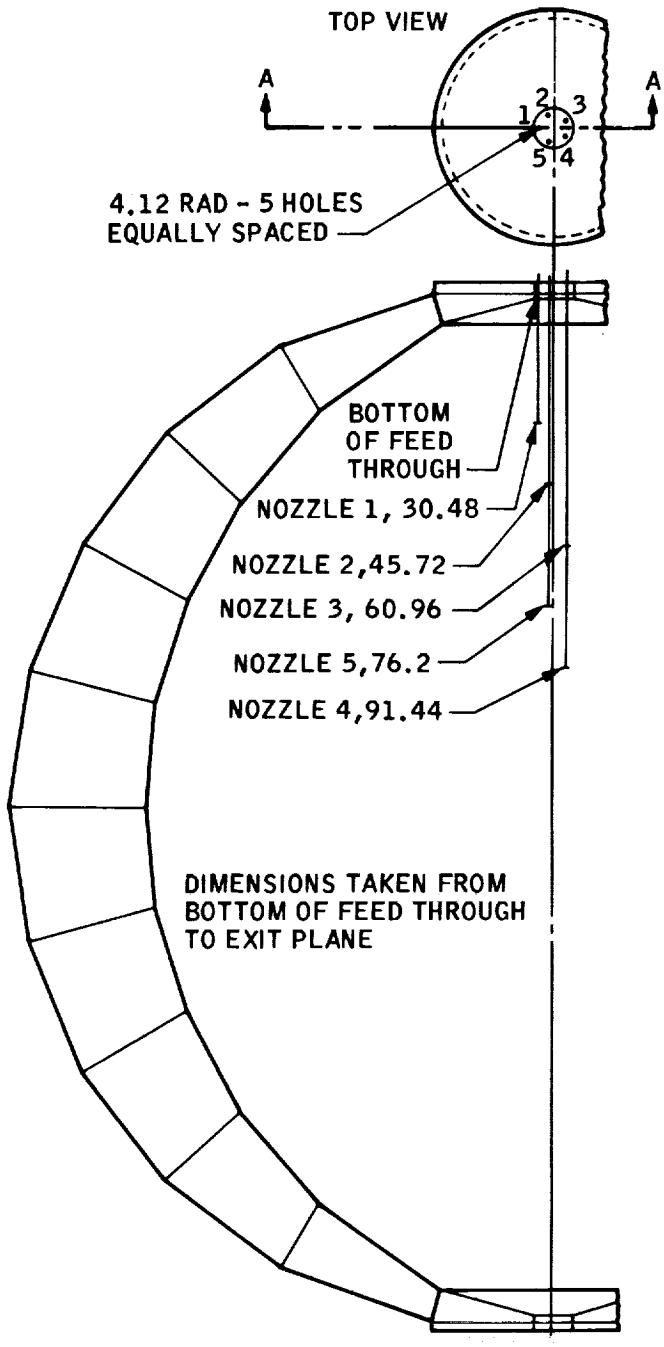

Fig. 4. Arrangement of the 5 plenum-nozzle assembly units in the Molsink (all dimensions are in cm)

$$\Delta f = C_M \Delta M + C_T \Delta T$$

$$C_M = \phi(T, \text{CUT ANGLES})$$

$$C_T = \psi(T, \text{CUT ANGLES})$$

$$\text{If } C_T \approx 0, \quad \Delta M = \frac{\Delta f}{F_c^2} \times 4.35 \times 10^{-7}$$

ΔM (gm/cm^2)

Δf (Hz)

F_c (MHz)

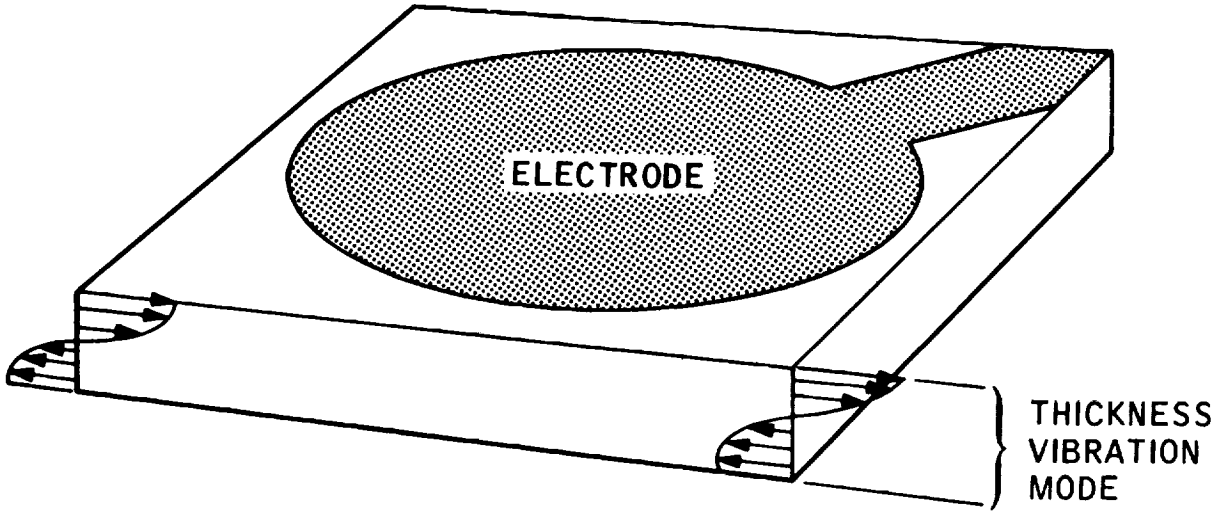

Fig. 5. Quartz crystal, electrodes, and demonstration of the thickness vibration mode

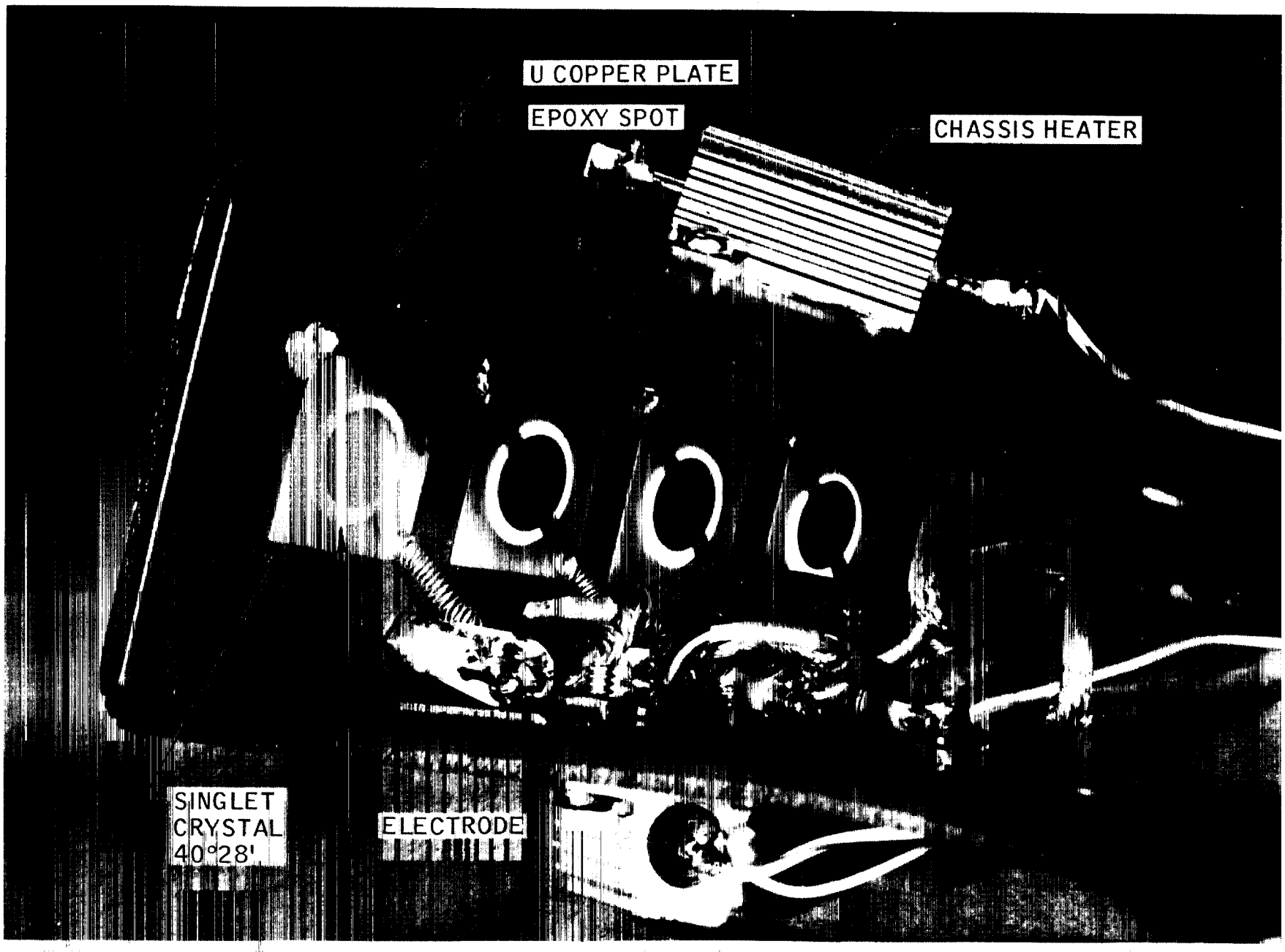

Fig. 6a. Rear view of 4 cryogenic crystals and other components mounted on a common chassis

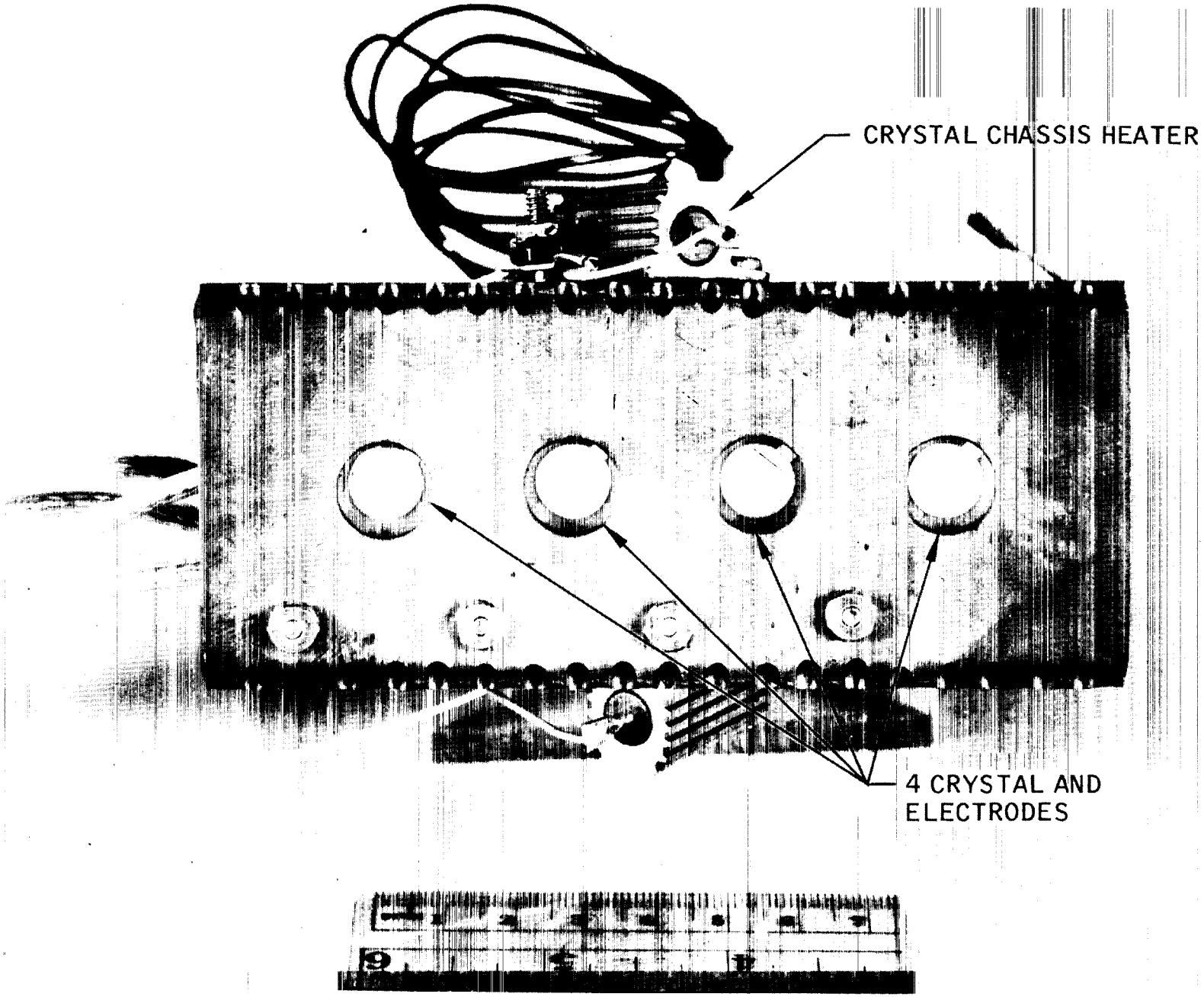

Fig. 6b. Side of the crystals facing the nozzles

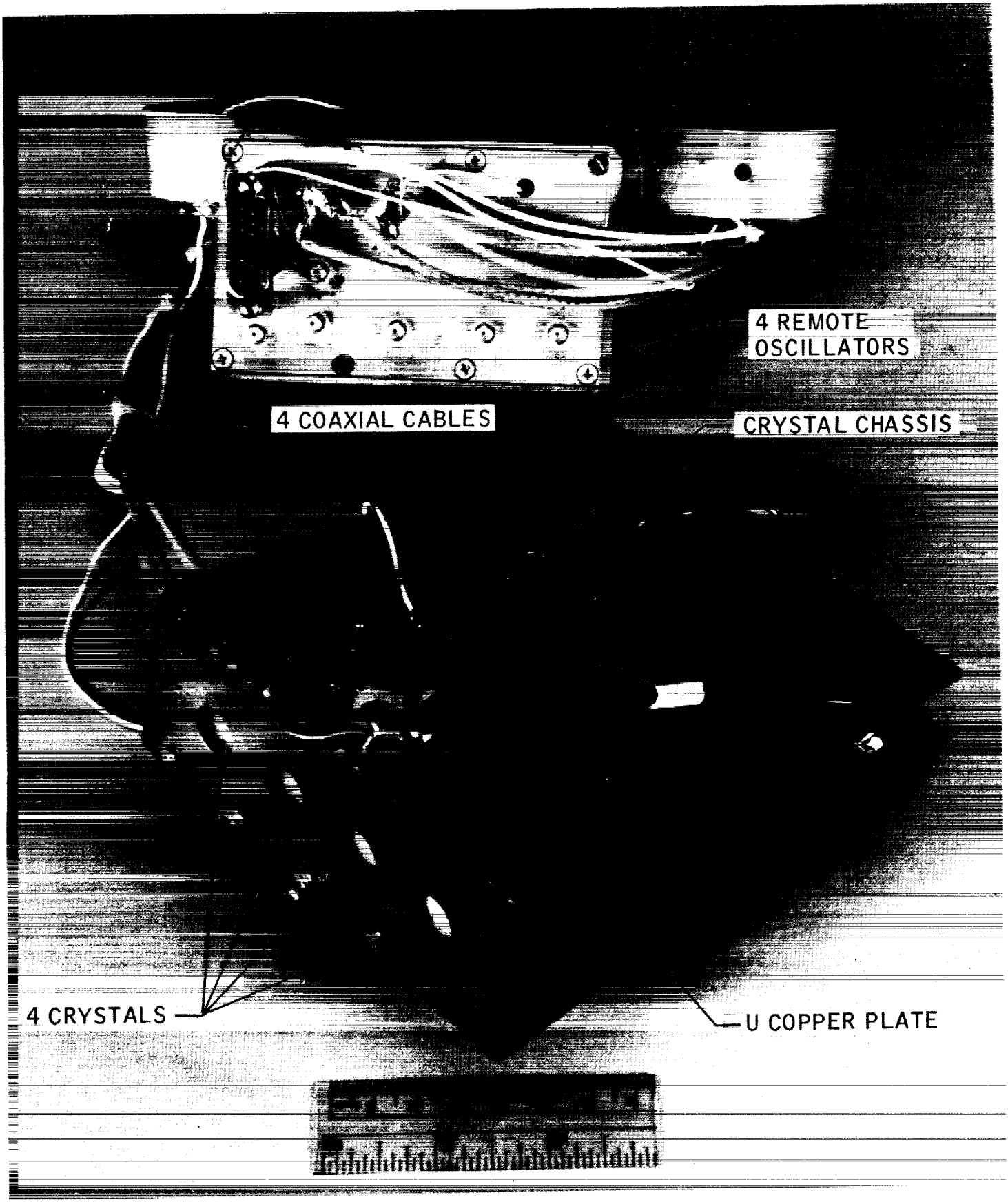

Fig. 6c. Crystal chassis and the remote oscillators block

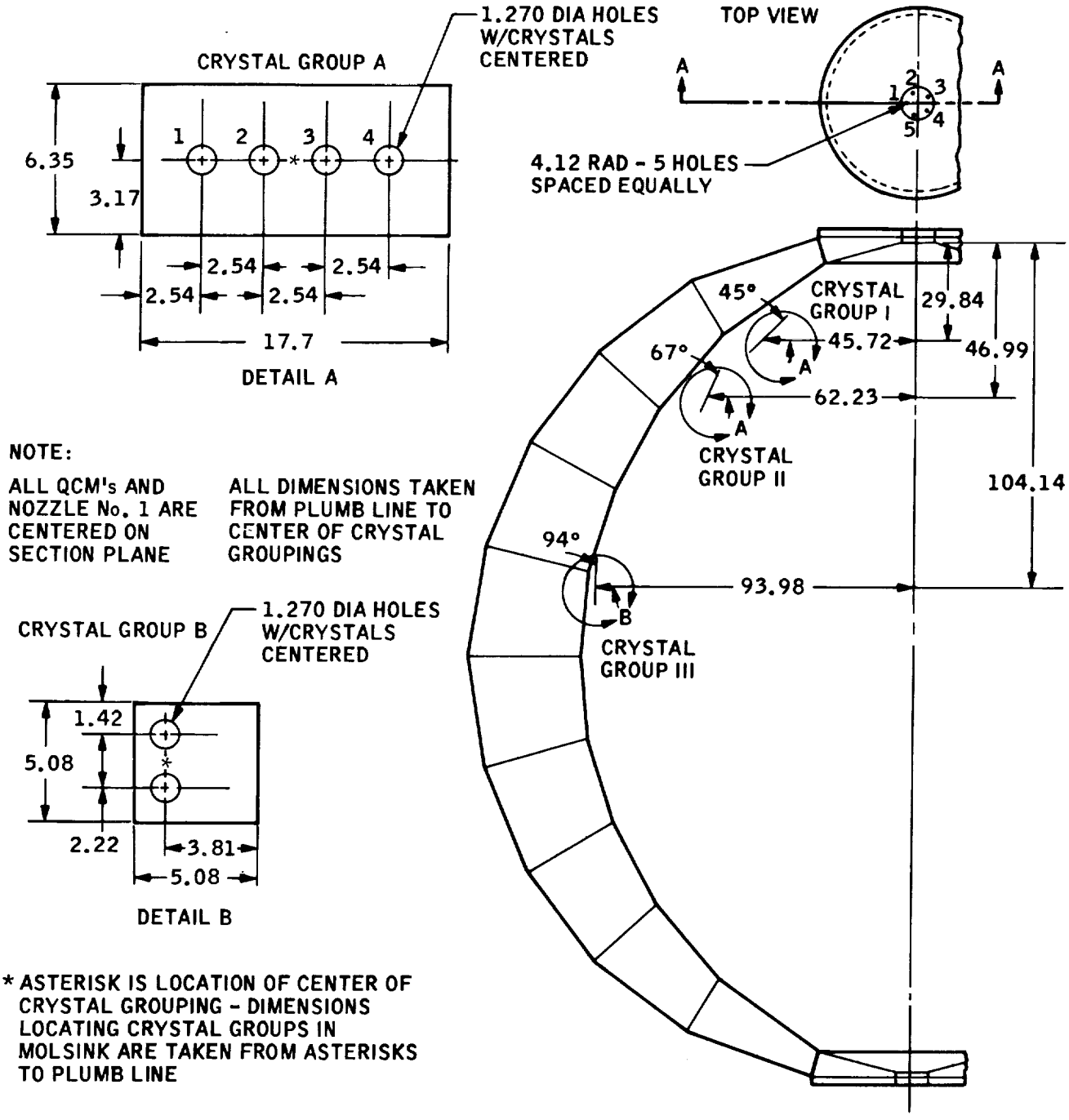

Fig. 7. Location and position of the QCM units in the Molsink chamber (all dimensions are in cm)

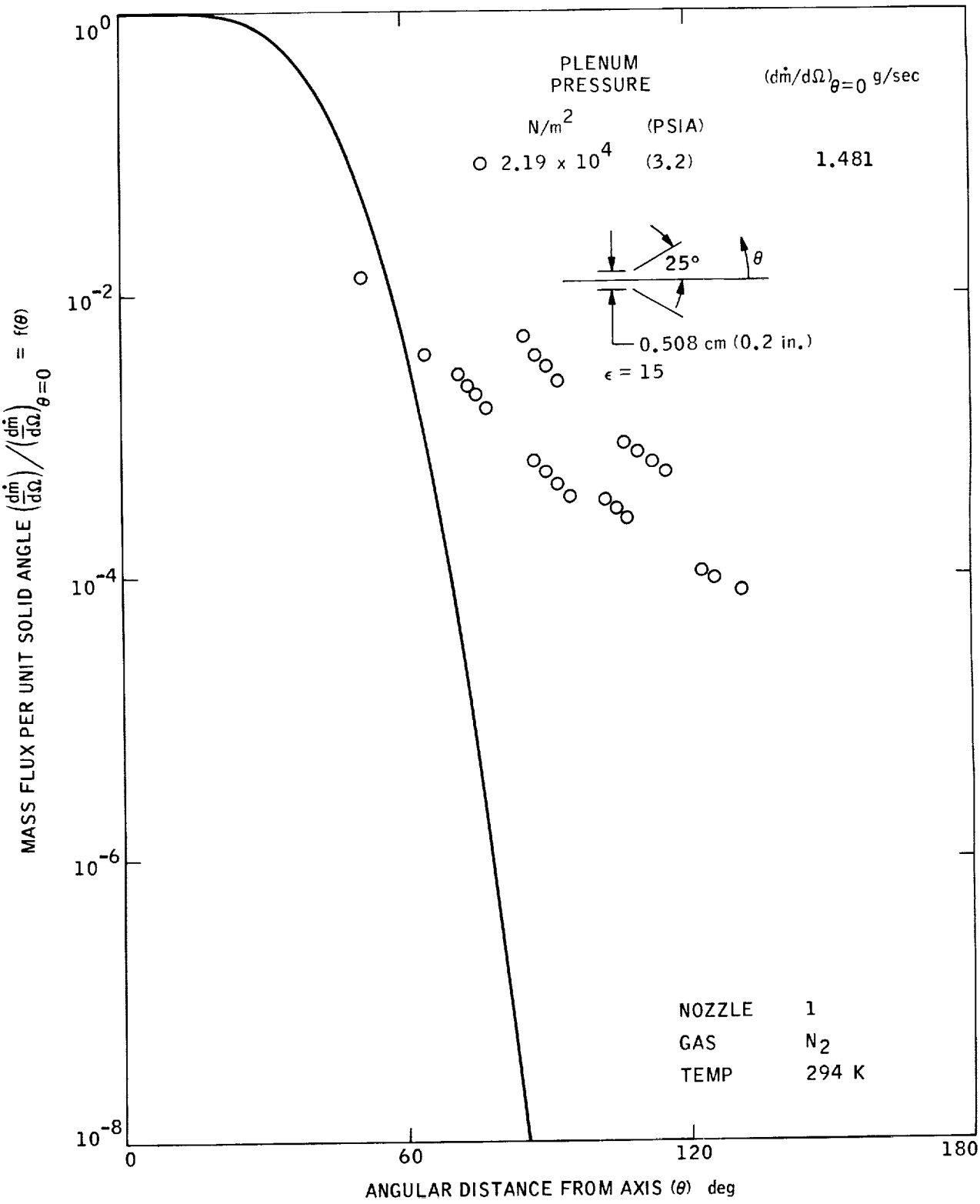

Fig. 8. Mass flux measurement data reduced and compared with the Hill and Draper approximation for Nozzle 1 and N_2 gas

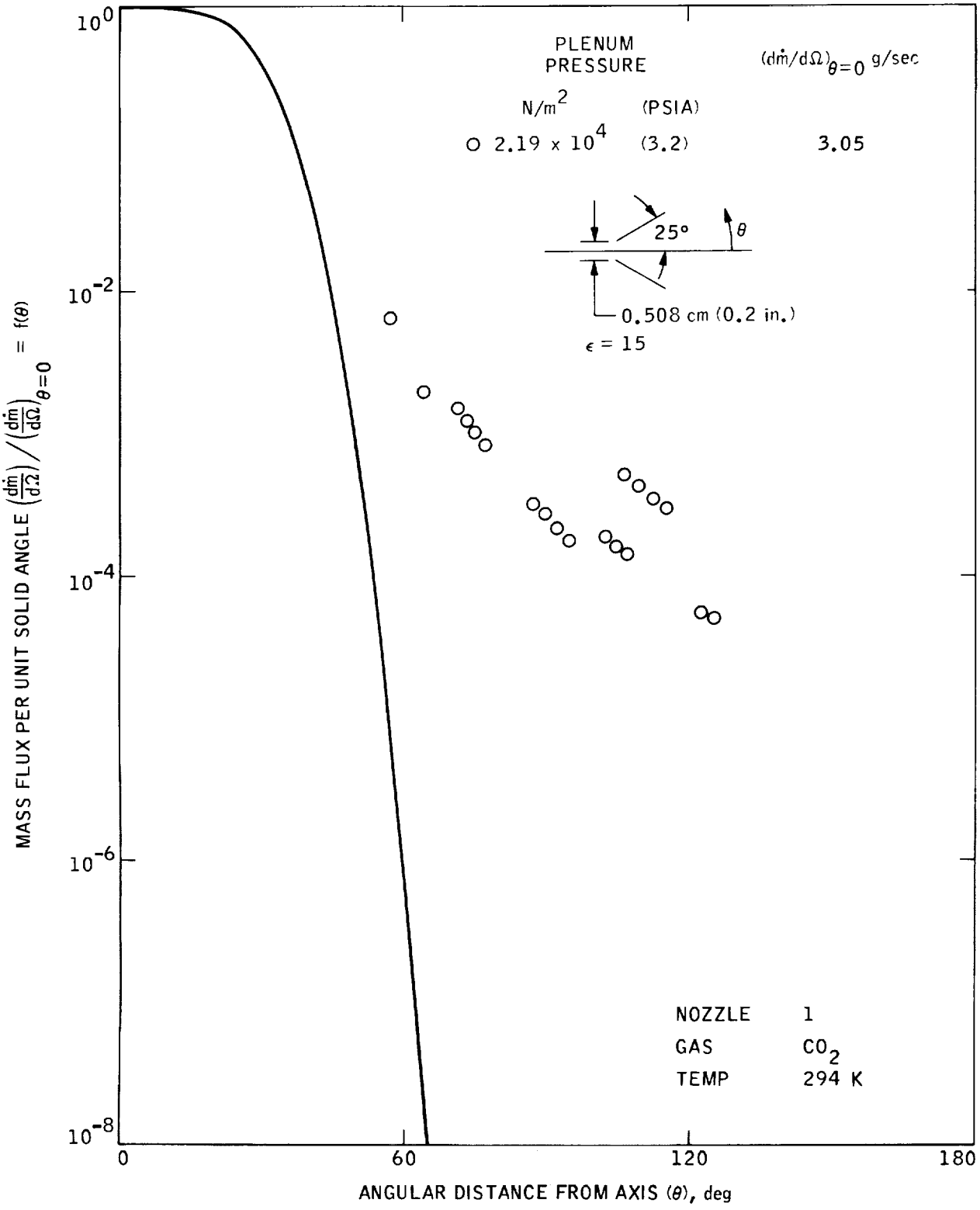

Fig. 9. Mass flux measurement data reduced and compared with the Hill and Draper approximation for Nozzle 1 and CO_2 gas

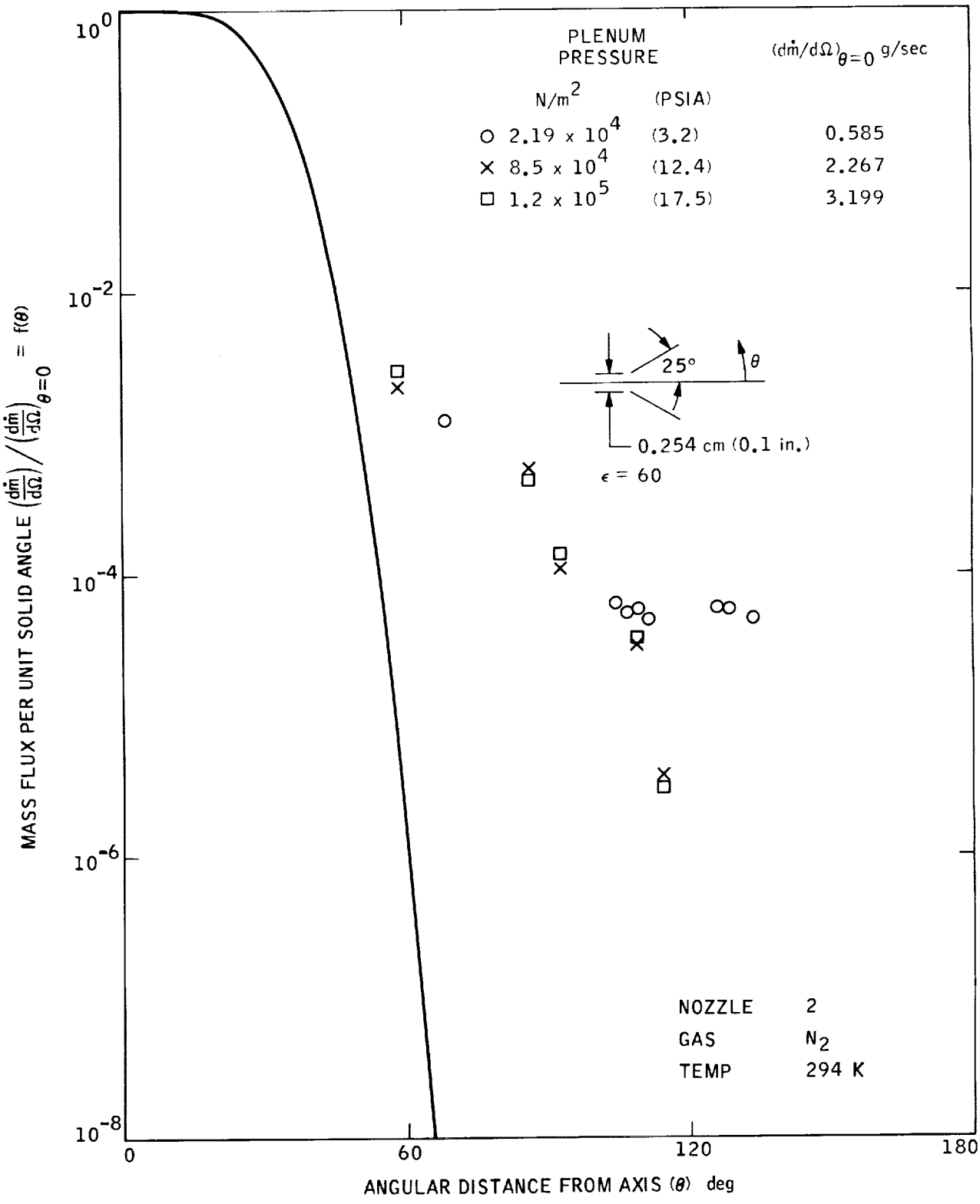

Fig. 10. Mass flux measurement data reduced and compared with the Hill and Draper approximation for Nozzle 2 and N_2 gas

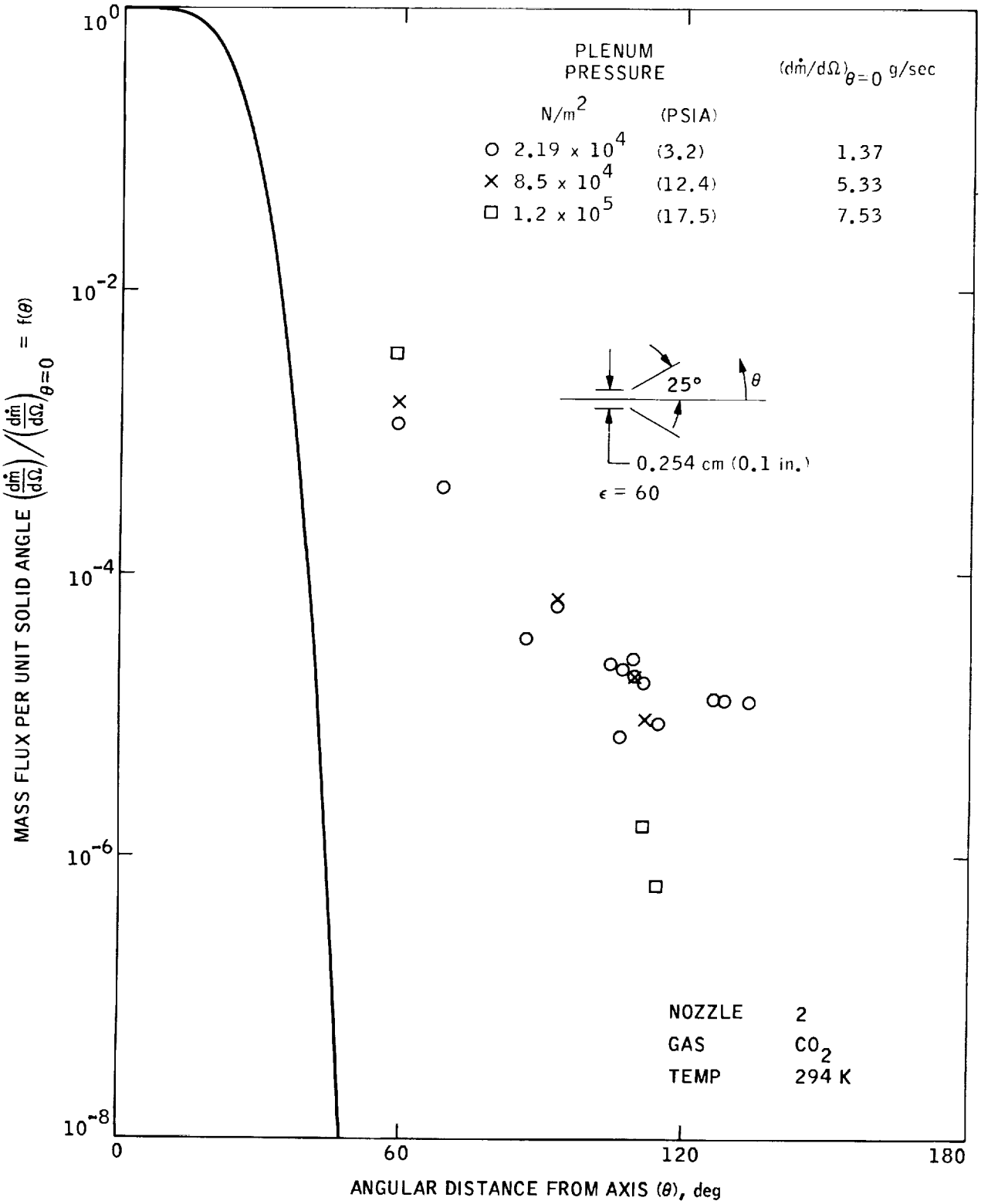

Fig. 11. Mass flux measurement data reduced and compared with the Hill and Draper approximation for Nozzle 2 and CO_2 gas

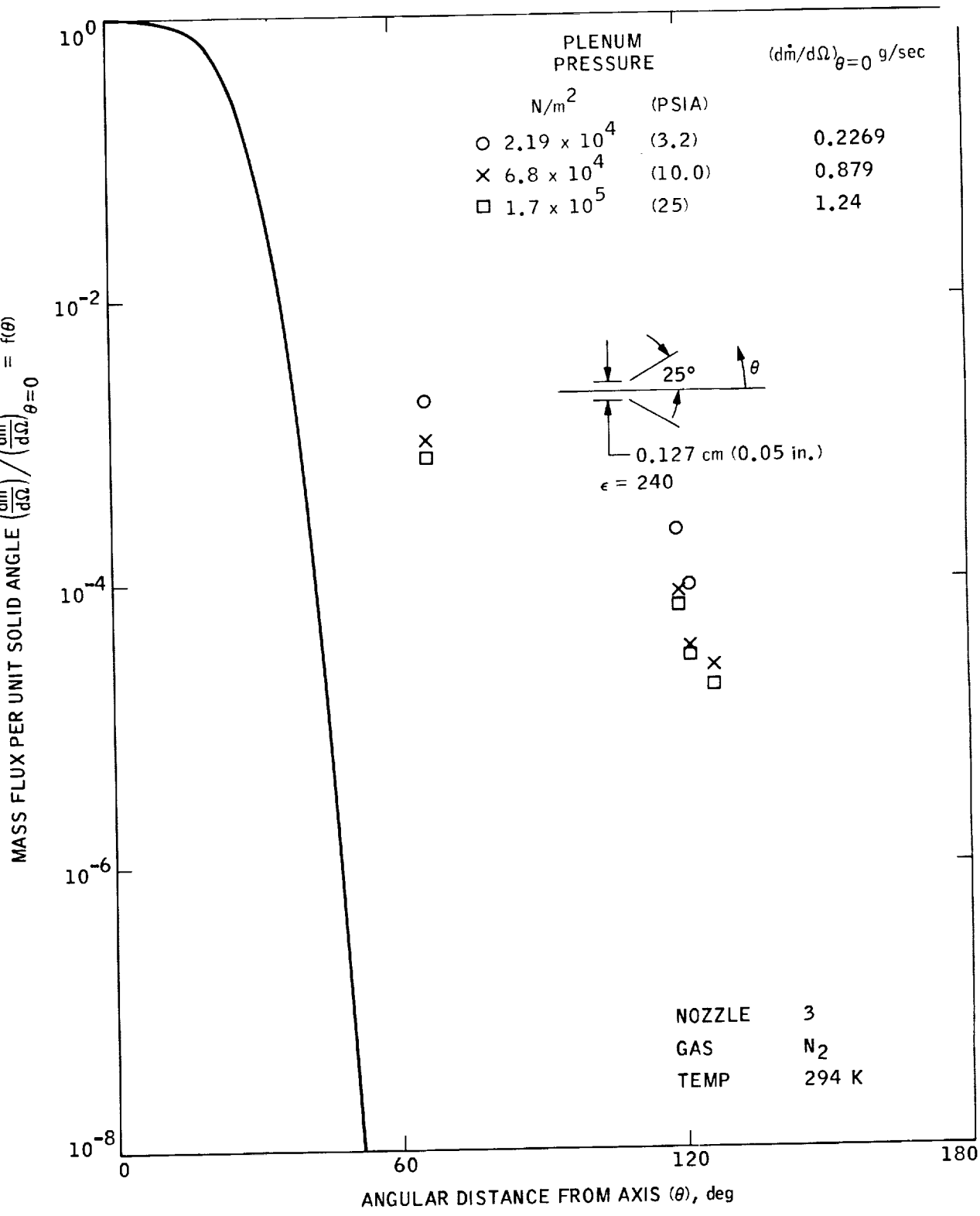

Fig. 12. Mass flux measurement data reduced and compared with the Hill and Draper approximation for Nozzle 3 and N_2 gas

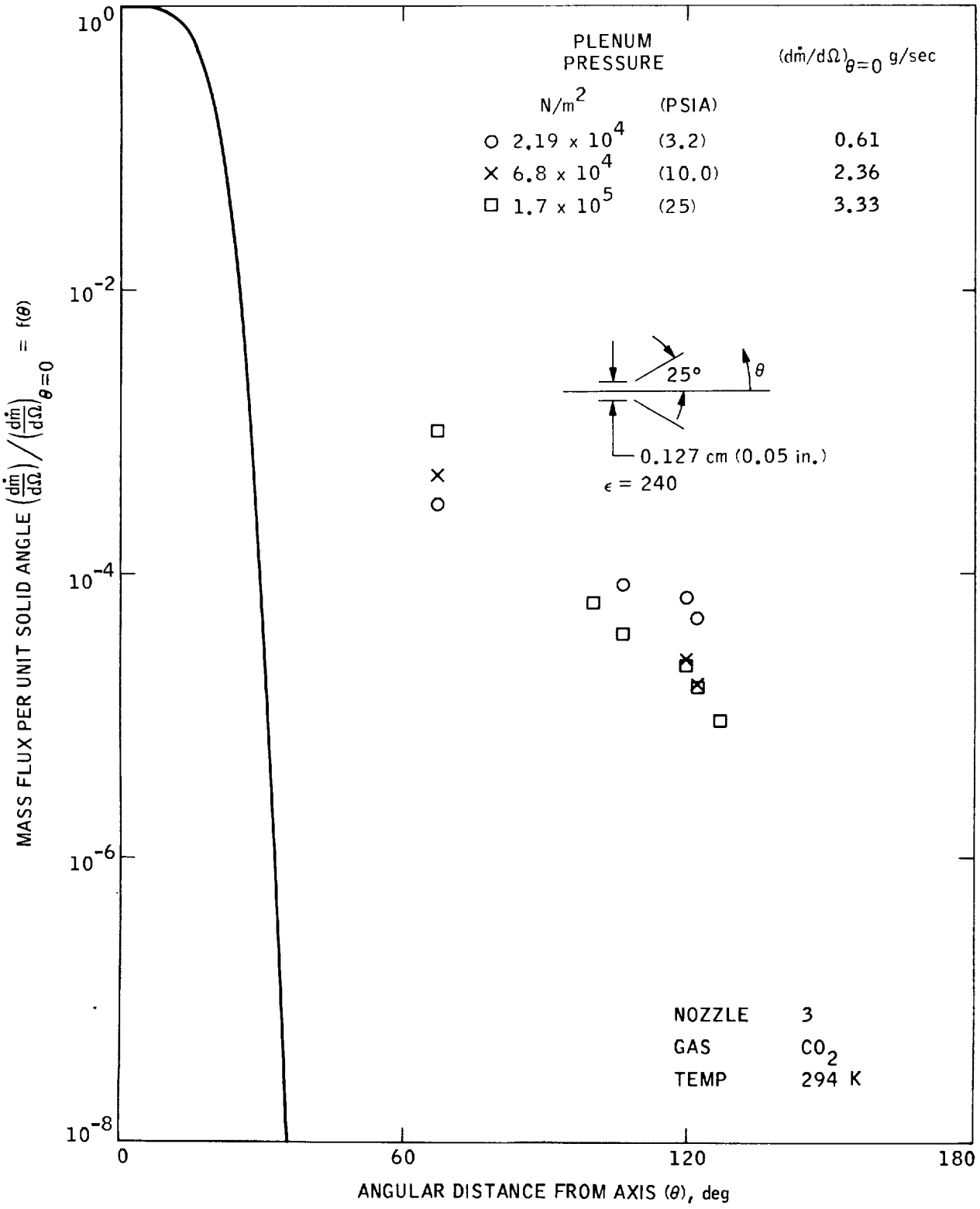

Fig. 13. Mass flux measurement data reduced and compared with the Hill and Draper approximation for Nozzle 3 and CO_2 gas

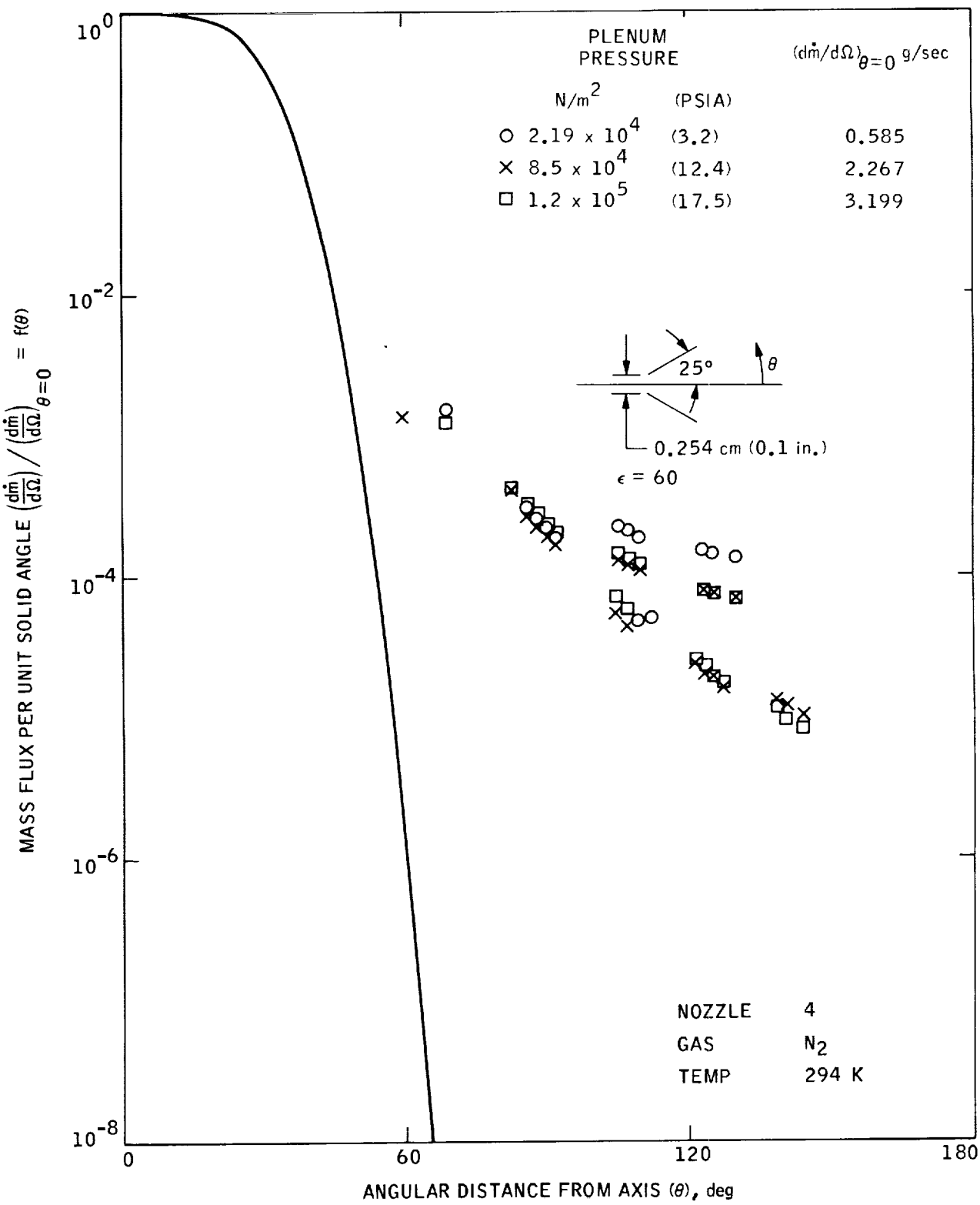

Fig. 14. Mass flux measurement data reduced and compared with the Hill and Draper approximation for Nozzle 4 and N_2 gas

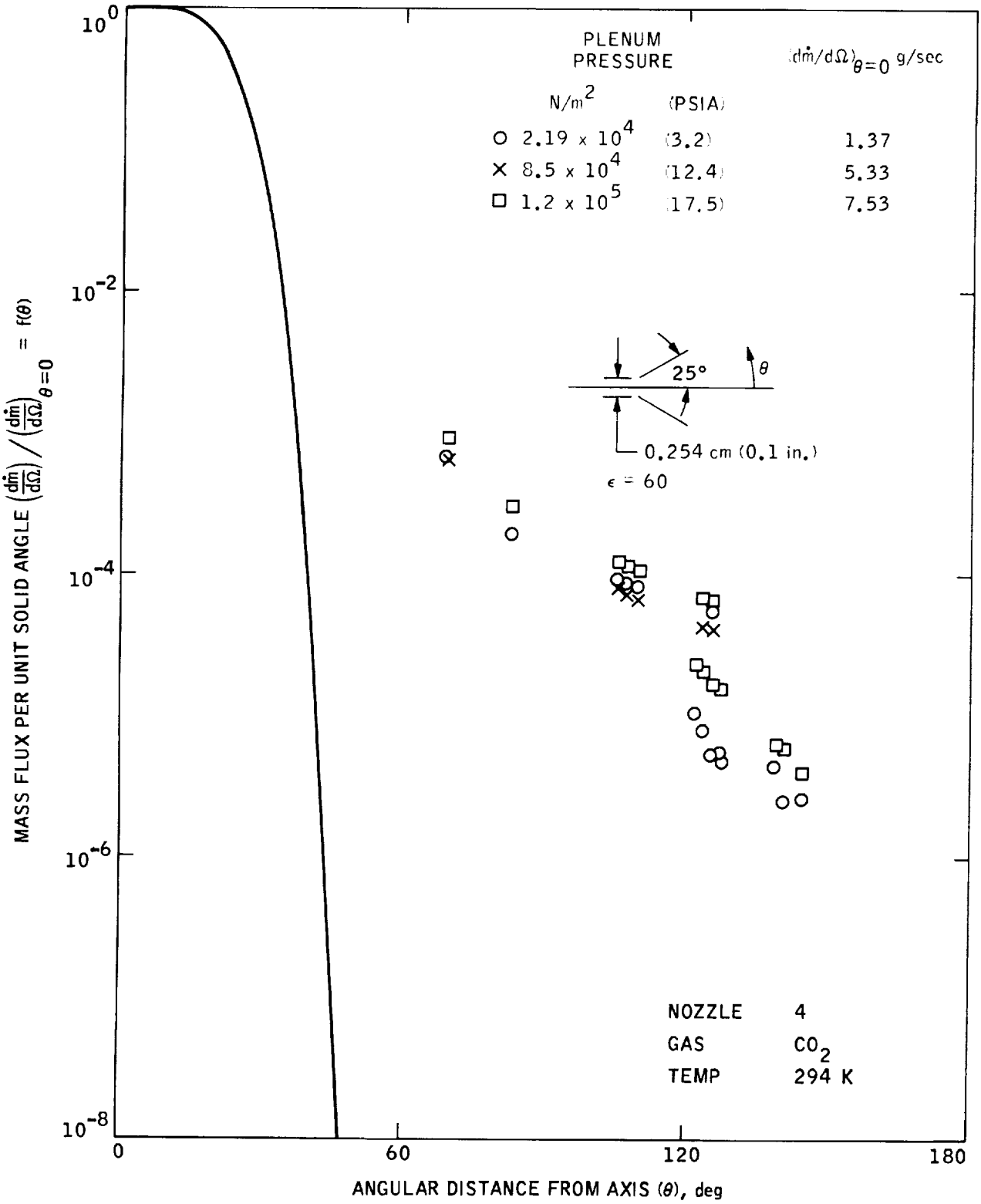

Fig. 15. Mass flux measurement data reduced and compared with the Hill and Draper approximation for Nozzle 4 and CO_2 gas

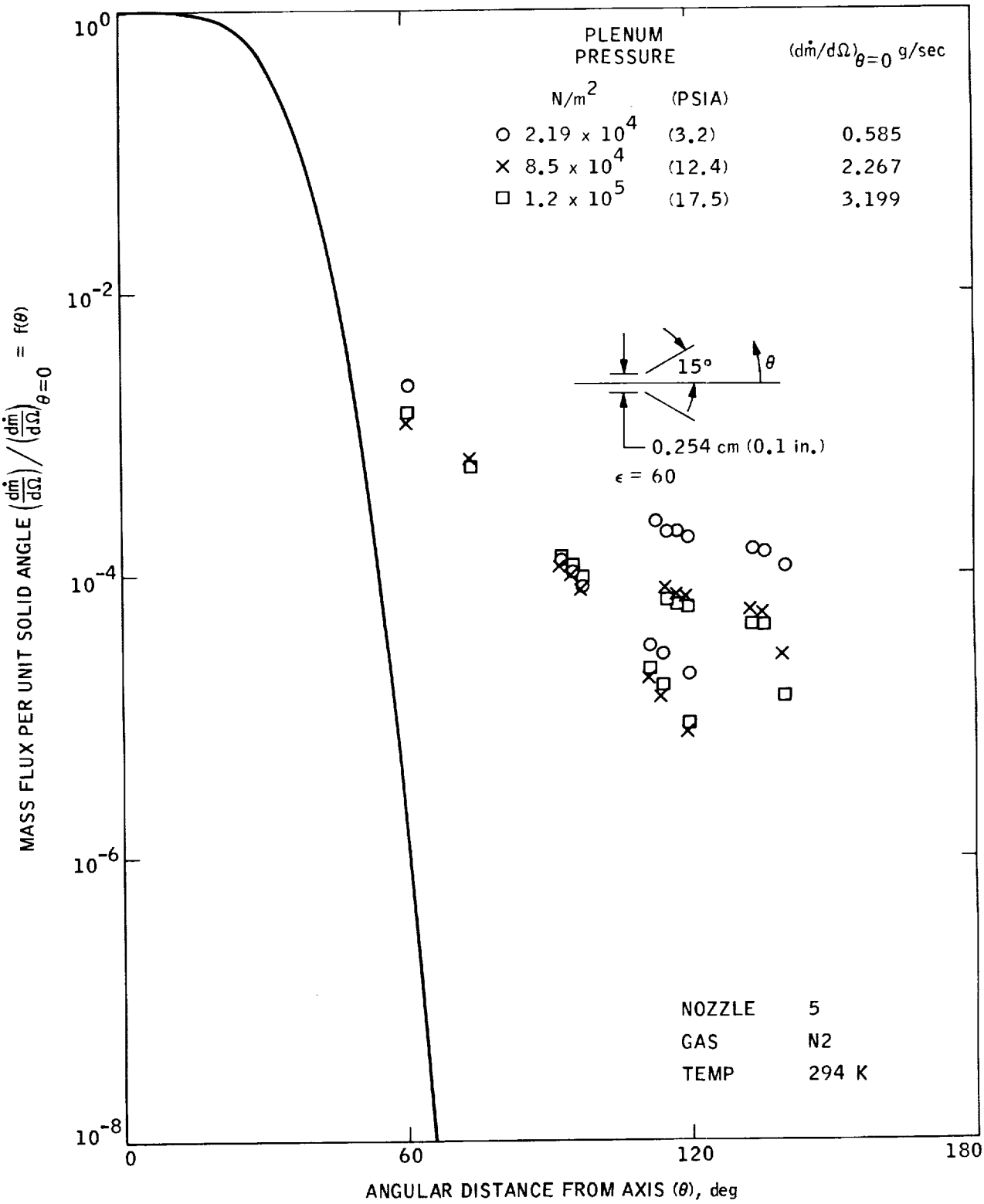

Fig. 16. Mass flux measurement data reduced and compared with the Hill and Draper approximation for Nozzle 5 and N_2 gas

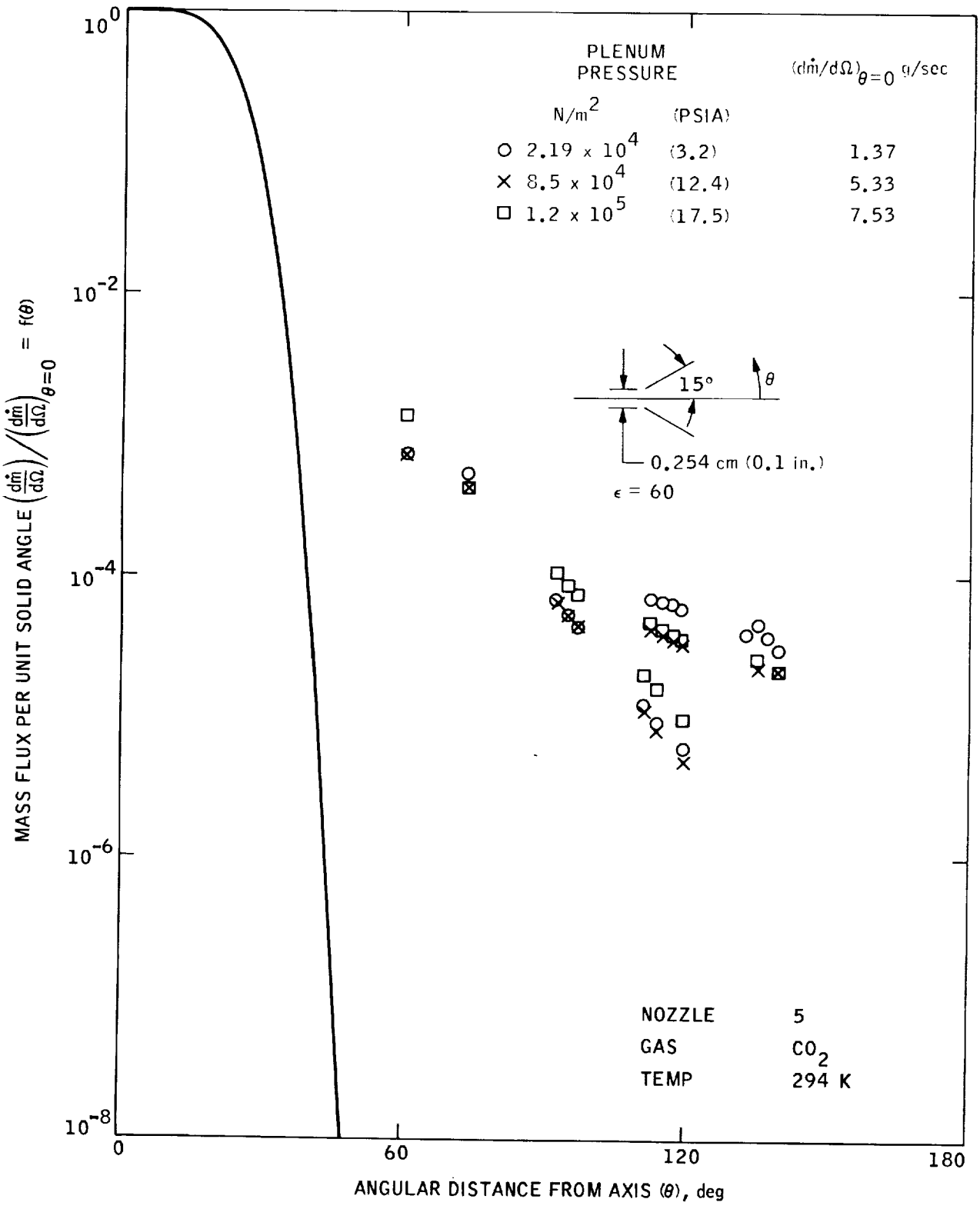

Fig. 17. Mass flux measurement data reduced and compared with the Hill and Draper approximation for Nozzle 5 and CO_2 gas

NASA — JPL — Coml., L.A., Calif.